Beam-Recoil Polarization Transfer in the Nucleon Resonance Region in the Exclusive $\vec{e}p \to e'K^+\vec{\Lambda}$ and $\vec{e}p \to e'K^+\vec{\Sigma}^0$ Reactions at CLAS

D.S. Carman,[1] B.A. Raue,[2] K.P. Adhikari,[26] M.J. Amaryan,[26] M. Anghinolfi,[15] H. Baghdasaryan,[33] M. Battaglieri,[15] M. Bellis,[7] A.S. Biselli,[12] C. Bookwalter,[13] D. Branford,[11] W.J. Briscoe,[16] W.K. Brooks,[31,1] V.D. Burkert,[1] P.L. Cole,[18,1] P. Collins,[4] V. Crede,[13] A. Daniel,[27] N. Dashyan,[34] R. De Vita,[15] E. De Sanctis,[14] A. Deur,[1] S. Dhamija,[2] C. Djalali,[30] G.E. Dodge,[26] P. Eugenio,[13] G. Fedotov,[22] S. Fegan,[17] A. Fradi,[28] M.Y. Gabrielyan,[2] K.L. Giovanetti,[20] F.X. Girod,[1] W. Gohn,[10] A. Gonenc,[2] R.W. Gothe,[30] H. Hakobyan,[31,34] C. Hanretty,[13] N. Hassall,[17] K. Hicks,[27] M. Holtrop,[24] Y. Ilieva,[30] D.G. Ireland,[17] H.S. Jo,[28] J.R. Johnstone,[17] P. Khetarpal,[29] W. Kim,[21] V. Kubarovsky,[1] V. Kuznetsov,[21] K. Livingston,[17] M. Mayer,[26] M.E. McCracken,[7] C.A. Meyer,[7] K. Mikhailov,[19] T. Mineeva,[10] M. Mirazita,[14] V. Mokeev,[22,1] B. Moreno,[28] K. Moriya,[7] M. Moteabbed, [2] P. Nadel-Turonski,[8] S. Niccolai,[28] M.R. Niroula,[26] M. Osipenko,[15,22] A.I. Ostrovidov,[13] K. Park,[1,30] S. Park,[13] E. Pasyuk,[4] O. Pogorelko,[19] J.W. Price,[6] D. Protopopescu,[17] G. Ricco,[15] M. Ripani,[15] B.G. Ritchie,[4] G. Rosner,[17] P. Rossi,[14] F. Sabatié,[5] M.S. Saini,[13] C. Salgado,[25] D. Sayre,[27] D. Schott,[2] R.A. Schumacher,[7] H. Seraydaryan,[26] Y.G. Sharabian,[1] D.I. Sober,[8] D. Sokhan,[11] S. Stepanyan,[1] S.S. Stepanyan,[21] S. Strauch,[30] M. Taiuti,[15] D.J. Tedeschi,[30] S. Tkachenko,[26] M. Ungaro,[10] M.F. Vineyard,[32] E. Wolin,[1] M.H. Wood,[30] J. Zhang,[26] B. Zhao,[10]

(CLAS Collaboration)

[1] *Thomas Jefferson National Accelerator Laboratory, Newport News, Virginia 23606*

[2] *Florida International University, Miami, Florida 33199*

[3] *Argonne National Laboratory, Argonne, Illinois 60439*

[4] *Arizona State University, Tempe, Arizona 85287*

[5] *CEA-Saclay, DAPNIA-SPhN, F91191 Gif-sur-Yvette Cedex, France*

[6] *California State University, Dominguez Hills, Carson, CA 90747*

[7] *Carnegie Mellon University, Pittsburgh, Pennsylvania 15213*

[8] *Catholic University of America, Washington, D.C. 20064*

[9] *Christopher Newport University, Newport News, Virginia 23606*

[10] *University of Connecticut, Storrs, Connecticut 06269*

[11] *Edinburgh University, Edinburgh EH9 3JZ, United Kingdom*

[12] *Fairfield University, Fairfield CT 06824*

[13] *Florida State University, Tallahasee, Florida 32306*

[14] *INFN, Laboratori Nazionali di Frascati, 00044 Frascati, Italy*

[15] *INFN, Sezione di Genova and Dipartimento di Fisica, Università di Genova, 16146 Genova, Italy*

[16] *The George Washington University, Washington, DC 20052*

[17] *University of Glasgow, Glasgow G12 8QQ, United Kingdom*

[18] *Idaho State University, Pocatello, Idaho 83209*

[19] *Institute of Theoretical and Experimental Physics, Moscow, 117259, Russia*

[20] *James Madison University, Harrisonburg, Virginia 22807*

[21] *Kyungpook National University, Daegu 702-701, South Korea*

[22] *Skobeltsyn Nuclear Physics Institute, 119899 Moscow, Russia*

[23] *Moscow State University, 119899 Moscow, Russia*

[24] *University of New Hampshire, Durham, New Hampshire 03824*

[25] *Norfolk State University, Norfolk, Virginia 23504*

[26] *Old Dominion University, Norfolk, Virginia 23529*

[27] *Ohio University, Athens, Ohio 45701*

[28] *Institut de Physique Nucleaire d'ORSAY, IN2P3, BP1, 91406 Orsay, France*

[29] *Rensselaer Polytechnic Institute, Troy, New York 12180*

[30] *University of South Carolina, Columbia, South Carolina 29208*

[31] *Universidad Técnica Federico Santa María, Valparaiso, Chile*

[32] *Union College, Schenectady, NY 12308*

[33] *University of Virginia, Charlottesville, Virginia 22901 and*

[34] *Yerevan Physics Institute, 375036 Yerevan, Armenia*

(Dated: April 21, 2009)

Beam-recoil transferred polarizations for the exclusive $\vec{e}p \to e'K^+\vec{\Lambda},\vec{\Sigma}^0$ reactions have been measured using the CLAS spectrometer at Jefferson Laboratory. New measurements have been completed at beam energies of 4.261 and 5.754 GeV that span a range of momentum transfer Q^2 from 0.7 to 5.4 GeV^2, invariant energy W from 1.6 to 2.6 GeV, and the full center-of-mass angular range of the K^+ meson. These new data add to the existing CLAS $K^+\Lambda$ measurements at 2.567 GeV, and provide the first-ever data for the $K^+\Sigma^0$ channel in electroproduction. Comparisons of the data with several theoretical models are used to study the sensitivity to s-channel resonance contributions and the underlying reaction mechanism. Interpretations within two semi-classical partonic models are made to probe the underlying reaction mechanism and the $s\bar{s}$ quark-pair creation dynamics.

PACS numbers: 13.88.+e, 14.40.aq, 14.20.Gk, 14.20.Jn

I. INTRODUCTION

An important requirement to better understand the structure of the nucleon is to map out its spectrum of excited states. However, deciphering the data to understand the resonance excitations has been limited both by the data itself and the current state of existing theories. Ideally we should expect the fundamental theory of the strong interaction, quantum chromodynamics (QCD), to provide a prediction for the nucleon excitation spectrum. However, due to the non-perturbative nature of QCD at the relevant energies, this idea has not yet been fully realized. Thus we have looked instead to effective models of QCD, such as constituent quark models, to gain some insight. Present quark model calculations of the nucleon spectrum have predicted more states than have been seen experimentally [1]. This has been termed the "missing" resonance problem, and the existence of these states is tied in directly with the underlying degrees of freedom of the nucleon that govern hadronic production at moderate energies [2].

Most of our current understanding of nucleon resonances comes from reactions involving pions in the initial and/or final states. Koniuk and Isgur suggested that the missing states might be revealed in decays to channels where mesons other than pions or multiple pions are in the final state [3]. Indeed, there are indications from theory that some missing states have a similar probability of decaying into channels such as ωN, ηN, $\pi\pi N$, and KY ($Y = \Lambda, \Sigma$) compared to the πN channel [1, 4]. As baryon resonances have large widths and are often overlapping, studies of different final states provide important complementary cross checks in quantitatively understanding the contributing amplitudes.

In this work we study the electroproduction of strange final states. While electromagnetic production of KY final states has a much lower cross section than hadronic production reactions, the use of an electromagnetic probe has a distinct advantage, namely that all electromagnetic quantities in the reaction amplitude can be straightforwardly expressed in the context of quantum electrodynamics. Furthermore, in addition to the different coupling constants compared to the πN channel (e.g. g_{KNY} vs. $g_{\pi NN}$), the study of the exclusive production of KY final states has another advantage in the search for missing resonances. The higher masses of the kaon and hyperons, compared to their non-strange counterparts, kinematically favor a two-body decay mode for states with masses near 2 GeV. Not only is this situation advantageous from an experimental viewpoint, but this also happens to be the mass region where the majority of the missing resonance states are expected to exist [1].

Although the two ground-state hyperons have the same valence quark structure (uds), they differ in isospin, such that intermediate N^* resonances can decay strongly to $K\Lambda$ final states, while both N^* and Δ^* decays can couple to

$K\Sigma$ final states. Existing studies of $N^* \to K\Lambda, K\Sigma$ and $\Delta^* \to K\Sigma$ decays have not yet provided extensive or precise information on the $N^*, \Delta^* \to KY$ couplings. To date, the Particle Data Group (PDG) only lists four N^* states with known couplings to $K\Lambda$ and no N^* states are listed that couple to $K\Sigma$ [5]; only a single Δ^* state is listed with coupling strength to $K\Sigma$. The current landscape as given by the PDG for $N^*, \Delta^* \to KY$ is given in Table I.

$N^* \to KY$				$\Delta^* \to K\Sigma$		
State	Rating	B.R. ($K\Lambda$)	B.R. ($K\Sigma$)	State	Rating	B.R. ($K\Sigma$)
$N^*(1650)\ S_{11}$	****	3 – 11%	–	$\Delta^*(1700)\ D_{33}$	****	–
$N^*(1675)\ D_{15}$	****	< 1%	–	$\Delta^*(1750)\ P_{31}$	*	–
$N^*(1680)\ F_{15}$	****	–	–	$\Delta^*(1900)\ S_{31}$	**	–
$N^*(1700)\ D_{13}$	***	< 3%	–	$\Delta^*(1905)\ F_{35}$	****	–
$N^*(1710)\ P_{11}$	***	5 – 25%	–	$\Delta^*(1910)\ P_{31}$	****	–
$N^*(1720)\ P_{13}$	***	1 – 15%	–	$\Delta^*(1920)\ P_{33}$	***	2.1%
$N^*(1900)\ P_{13}$	**	2.4%	–	$\Delta^*(1930)\ D_{35}$	***	–
$N^*(1990)\ F_{17}$	**	–	–	$\Delta^*(1940)\ D_{33}$	*	–
$N^*(2000)\ F_{15}$	**	–	–	$\Delta^*(1950)\ F_{37}$	****	–
				$\Delta^*(2000)\ F_{35}$	**	–

TABLE I: PDG listings for the coupling of N^* (Δ^*) states below 2 GeV to $K\Lambda$ and $K\Sigma$ ($K\Sigma$) [5]. The *Rating* column gives the PDG star rating for the N^* states and *B.R.* indicates the branching ratio.

Theoretically, there has been considerable effort during the past two decades to develop models for KY photo- and electroproduction. However, the present state of understanding is limited by a lack of precision data (Ref. [6] contains a brief review). Model fits to the cross section data are generally obtained at the expense of many free parameters, which makes it difficult to provide precise constraints. Moreover, cross section data alone are not sufficient to fully understand the reaction mechanism, as they represent only a portion of the full amplitude response. In this regard, measurements of spin observables are essential for continued theoretical development in this field. Fits to the limited available data lead to ambiguities and model dependence in interpreting the results. Polarization data can provide for improved constraints on the model parameters, increasing their discriminatory power and allow for a quantitative measure of whether or not new resonance states are required to explain these and other hyperon production data. One main issue involves discriminating resonant states from the non-resonant background and from effects caused by final-state interactions or channel-couplings instead of N^* and Δ^* contributions [7].

CLAS at Jefferson Laboratory (JLab) has provided photoproduction $K^+\Lambda$ and $K^+\Sigma^0$ recoil polarization data from the proton [8]. In addition, beam-recoil polarization transfer data from CLAS have been published for both $K^+\Lambda$ and $K^+\Sigma^0$ photoproduction [9] and $K^+\Lambda$ electroproduction [10] reactions on the proton. Data such as these that span both a wide energy and angular range and are essential to disentangle the resonant and non-resonant contributions

to the KY spectrum [7, 11]. This has been demonstrated in several recent amplitude-level analyses with channel couplings based on photoproduction data [12, 13, 14, 15, 16, 17, 18, 19]. Further progress is expected as data with broad coverage and smaller experimental uncertainties are made available (which includes new CLAS data with linearly polarized photon beams and polarized targets [20, 21, 22]).

In this work, we focus on measurements of spin transfer from a longitudinally polarized electron beam to the ground-state hyperons produced in the reactions $p(\vec{e}, e'K^+)\vec{\Lambda}$ and $p(\vec{e}, e'K^+)\vec{\Sigma}^0$ at beam energies E_b of 4.261 and 5.754 GeV. This work represents a higher-statistics follow-up to the first data presented by CLAS in the $K^+\Lambda$ channel for an electron beam energy of 2.567 GeV [10], where the transferred Λ polarization was studied as a function of the invariant energy W and $\cos\theta_K^{c.m.}$ (the K^+ center-of-mass angle). The transferred polarization data for the $K^+\Sigma^0$ final state included here represent the first-ever published data for this observable in electroproduction.

From the polarization data in Ref. [10], the ratio of the longitudinal to transverse structure functions σ_L/σ_T for the $K^+\Lambda$ final state at $\theta_K^{c.m.} = 0^\circ$ was extracted for several W points near 1.8 GeV and Q^2 $\sim$0.7 GeV^2 [23]. These results indicated a ratio that was systematically smaller than previously published results using a Rosenbluth separation performed in Hall C at Jefferson Laboratory [24], albeit with large statistical uncertainties. In fact, the data were consistent with zero within the experimental uncertainties, which would imply a small longitudinal structure function, and hence, a small longitudinal coupling of the virtual photon. The results of Ref. [23] are expanded upon in this work with larger data sets that reduce uncertainties in the extrapolation to $\theta_K^{c.m.} = 0^\circ$. The new data presented include three data points near W=1.9 GeV with an average Q^2 of $\sim$1.6 GeV^2 and three data points near W=2.0 GeV with an average Q^2 of $\sim$2.5 GeV^2.

Using a semi-classical partonic framework, the CLAS polarization data in Ref. [10] were shown to support a description where the spin properties of the quark-pair creation operator might be responsible for the observed trends in the Λ polarization. This framework indicated that the quark-pair creation operator dominating the reaction produces the $s\bar{s}$ pair with spins anti-aligned. This finding, if confirmed, has important implications since many, if not most, calculations of hadron spectroscopy use a $^3P_0$ operator to calculate the transition to the final-state particles [25]. In this work, the angular distribution of the transferred polarization is studied with greater precision than in Ref. [10] and compared against two semi-classical partonic models that lead to quite different predictions regarding the $K^+\Lambda$ reaction mechanism and the quark-pair creation dynamics. The first is the model from Ref. [10]. The second assumes the reaction proceeds from an $s\bar{s}$ quark-pair with the quark spins aligned. The main differences between the models are discussed and a possible experiment to discriminate between them is proposed.

The organization for the remainder of this paper is as follows. In Sections II and III, the theoretical models to be compared with the measurements are briefly introduced and the relevant formalism for the polarization measurements is provided. Section IV gives a detailed description of how the polarization is extracted and Section V gives details regarding the analysis cuts and corrections to the data. Section VI details the sources of systematic uncertainty. Section VII contains the physics results, with the presentation of the $K^+\Lambda$ and $K^+\Sigma^0$ polarization transfer data in Sections VII A and VII B, respectively, the new σ_L/σ_T extraction in Section VII C, and comparisons of the data to the newly developed partonic models in Section VII D. Finally, we present a summary of this work and our conclusions in Section VIII.

II. THEORETICAL MODELS

While the QCD description of quark interactions and pair creation is well accepted at high energies, the situation is considerably more complex in the low-energy nucleon resonance region due to the non-perturbative nature of the theory. In order to arrive at any theoretical expectations for the transferred polarization, effective models must be employed that ultimately represent approximations to QCD. This analysis highlights three different theoretical model approaches. The first is a traditional hadrodynamic model, the second is based on kaon Regge trajectory exchange, and the third is a hybrid Regge plus resonance approach.

A. Hadrodynamic models

Hadrodynamic models provide a description of the reaction based on an effective Lagrangian constructed from tree-level Born and extended Born terms in the s, t, and u reaction channels (see Fig. 1). The Born diagrams include the exchange of the proton, kaon, and ground-state hyperons, while the extended Born diagrams include the exchange of the associated excited states. This description of the interaction, which involves only first-order terms, is sensible as the incident and outgoing electrons interact rather weakly with the hadrons. A complete description of the physics processes requires taking into account all possible channels that could couple to the initial and final states, but the advantages of the tree-level approach are to limit complexity and to identify the dominant trends. The drawback in this class of models is the large number of hadrons that can contribute in the intermediate state of the reaction. Depending on which set of resonances a given model includes, very different conclusions about the strengths of the contributing diagrams may be reached.

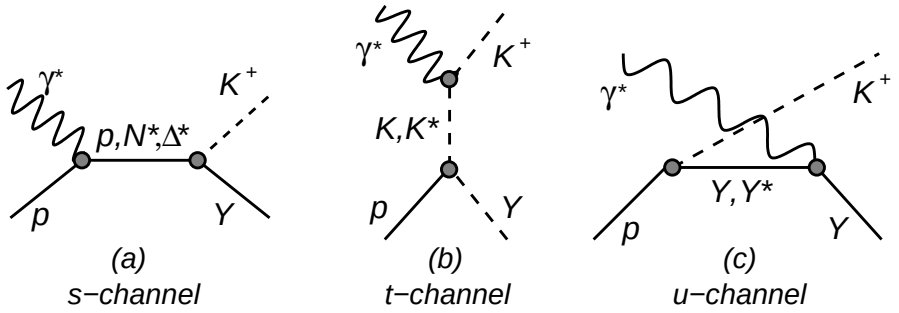

FIG. 1: Tree-level diagrams contributing to the KY reactions: (a) s-channel exchanges, (b) t-channel exchanges, and (c) u-channel exchanges.

The hadrodynamic model employed in this work is from Mart and Bennhold [26] (referred to here as MB). The s-channel terms included in this model are listed in Table II. The coupling strengths have been determined by a simultaneous fit to low-energy $K^-p \to \gamma Y$ and $\gamma^{(*)}p \to K^+Y$ data, by adding the non-resonant Born terms with a number of resonances, leaving the coupling constants as free parameters. The coupling constants are required to respect the limits imposed by SU(3), allowing for a symmetry breaking at the level of about 20%. In this model, the inclusion of hadronic form factors leads to a breaking of gauge invariance that is restored by the inclusion of counter terms [26]. The model has been compared to the CLAS photoproduction [8, 27] and electroproduction data [6] and provides for a fair description of those results, although no CLAS data were employed in the model fits.

	MB		RPR	
State	$K^+\Lambda$	$K^+\Sigma^0$	$K^+\Lambda$	$K^+\Sigma^0$
$N^*(1650)$ (S_{11})	*	*	*	*
$N^*(1710)$ (P_{11})	*	*	*	*
$N^*(1720)$ (P_{13})	*	*	*	*
$N^*(1900)$ (P_{13})			*	*
$N^*(1900)$ (D_{13})	*	*	*	
$N^*(1900)$ (P_{11})			*	
$\Delta^*(1700)$ (D_{33})				*
$\Delta^*(1900)$ (S_{31})		*		*
$\Delta^*(1910)$ (P_{31})		*		*
$\Delta^*(1920)$ (P_{31})				*

TABLE II: List of s-channel resonant terms included in the MB model [26] and the Regge plus resonance (RPR) model [7] included in this work. Note that the RPR model has two variants that include either a $D_{13}(1900)$ or $P_{11}(1900)$ state.

For $K^+\Lambda$ production, the MB model includes four baryon resonance terms. Near threshold, the steep rise of the cross section is accounted for with a core set of N^* states: $S_{11}(1650)$, $P_{11}(1710)$, $P_{13}(1720)$. To explain the broad bump in the energy dependence of the cross section seen by SAPHIR [28] and CLAS [6, 8, 27], the MB model includes a spin-3/2 $D_{13}(1900)$ resonance that was predicted in the quark model of Capstick and Roberts [1] to have a strong

coupling to the $K^+\Lambda$ channel, but which was not well established from existing pion-production data. For $K^+\Sigma^0$ production, the MB model includes the core N^* states and the Δ^* resonances $S_{31}(1900)$ and $P_{31}(1910)$. The model also includes $K^*(892)$ and $K_1(1270)$ exchanges for both KY final states, but does not include any u-channel diagrams.

The N^* states $S_{11}(1650)$, $P_{11}(1710)$, and $P_{13}(1720)$ are the only states listed by the Particle Data Group [5] with coupling strengths to $K\Lambda$ (see Table I). While the relevance of these core states in the $\gamma^{(*)}p \to K^+\Lambda$ reaction has long been considered a well-established fact, this set of states falls short of reproducing the experimental results in the region below W=2.0 GeV. Furthermore, two recent analyses have called the importance of the $P_{11}(1710)$ state into question [16, 18]. Beyond the core states, the PDG lists a two-star $P_{13}(1900)$ state as the sole established N^* near 1900 MeV. However, with a 500-MeV width, it appears unlikely that this state by itself can explain the structure(s) visible in the CLAS and SAPHIR cross sections, unless its parameters are significantly different than those given by the PDG. This has led to suggestions of a new (unconfirmed) N^* state in this mass region (e.g. the $D_{13}(1900)$ state in the MB model). However, the analysis of Saghai [29], using the same data sets employed for the MB model fits, concluded that by tuning the u-channel background processes involved in the $K^+\Lambda$ reaction, the need to include any states beyond the core set was removed. Note that the investigation of contributing N^* states to the KY reactions has typically been limited to spin $j < 5/2$ due to the expectations that higher-spin resonances do not significantly contribute to the reaction dynamics. [16, 30].

Moving beyond tree-level approaches to consider recent multipole and coupled-channels models has not led to dramatic new insights to the N^* spectrum. The multipole analysis by Mart and Sulaksono [31], as well as the coupled-channels models of Julia-Diaz *et al.* [17] and Sarantsev *et al.* [18] (which all employ CLAS photoproduction data in their fits), claim that a $D_{13}(1900)$ state is required by both the CLAS and SAPHIR $\gamma p \to K^+\Lambda$ data. However, the coupled-channels model of Ireland *et al.* [32] points to a $P_{11}(1840)$ state as a more likely candidate (although one or more of S_{11}, P_{11}, P_{13}, D_{13} are not ruled out). The fits of Julia-Diaz *et al.* [17] suggests a third S_{11} resonance might also be playing a role, while Sarantsev *et al.* [18] also require (in addition to a $D_{13}(1900)$) the presence of a $P_{11}(1840)$ and another D_{13} state at 2170 MeV. An extension of the coupled-channels model of Sarantsev *et al.* [18] by Avisovich *et al.* [19], which was the first model to include the CLAS photoproduction hyperon polarization transfer observables C_x and C_z [9], concluded that a $P_{13}(1900)$ state was also required to satisfactorily fit the data.

In the recent fits of the $\gamma p \to K^+\Sigma^0$ data, all N^* resonances found to be necessary to fit the $K^+\Lambda$ data have been included. However, the existing $K^+\Sigma^0$ database is much smaller than the $K^+\Lambda$ database, with significantly larger statistical uncertainties. Even with this situation, the recent coupled-channels models [17, 18, 19] indicate important

resonant contributions to the $K^+\Sigma^0$ final state from the N^* states $P_{11}(1840)$, $D_{13}(1870)$, $P_{13}(1885)$, and $D_{13}(2170)$, and from the Δ^* states $F_{35}(1905)$, $P_{33}(1940)$, and $F_{37}(1950)$.

Each different model has ambiguities that can be better constrained only by incorporating better quality data or including new experimental observables. Comparison of the models to the data can be used to provide indirect support for the existence of the different baryonic resonances and their branching ratios into the strange channels, as well as improved constraints on the phenomenology of the different strangeness production reactions.

B. Regge and regge plus resonance models

Our KY electroproduction data are also compared to the Reggeon-exchange model from Guidal, Laget, and Vanderhaeghen [33] (referred to here as GLV). This calculation includes no baryon resonance terms at all. Instead, it is based only on gauge-invariant t-channel K and K^* Regge-trajectory exchange. It therefore provides a complementary basis for studying the underlying dynamics of strangeness production. It is important to note that the Regge approach has far fewer parameters compared to the hadrodynamic models. These include the K and K^* form factors (assumed to be of a monopole form) and the coupling constants g_{KYN} and g_{K^*YN} (taken from photoproduction studies). The GLV model was fit to higher-energy photoproduction data where kaon exchanges dominate and extrapolated down to JLab energies. Furthermore, the use of Regge propagators eliminates the need to introduce strong form factors in the background terms, thus avoiding the gauge-invariance issues associated with traditional effective Lagrangian models.

The GLV Regge model reasonably accounts for the strength in the CLAS $K^+\Lambda$ differential cross sections and separated structure functions [6, 27]. Although the reasonable performance of a pure Regge description in this channel suggests a t-channel dominated process, there are obvious discrepancies with the data, indicative of s-channel strength. In the $K^+\Sigma^0$ channel, the same Regge description significantly underpredicts the differential cross sections and separated structure functions [6, 27]. The fact that the Regge model fares poorly when compared to the $K^+\Sigma^0$ data is indicative that this process has a much larger s-channel content compared to $K^+\Lambda$ production.

The final model included in this work is based on a tree-level effective field model for Λ and Σ^0 photoproduction from the proton. It differs from traditional isobar approaches in its description of the non-resonant diagrams, which involve the exchange of K and K^* Regge trajectories. A selection of s-channel resonances are then added to this background. This "Regge plus resonance" model (referred to here as RPR) [7] has the advantage that the background diagrams contain only a few parameters that are constrained by high-energy data where the t-channel processes dominate. In addition to the kaonic trajectories, the RPR model includes the s-channel resonances $S_{11}(1650)$, $P_{11}(1710)$, $P_{13}(1720)$,

and $P_{13}(1900)$ (see Table II). The model also includes either a $D_{13}(1900)$ or $P_{11}(1900)$ state in the $K^+\Lambda$ channel. In detailed comparisons with the separated structure functions [6, 34] and transferred polarization data from CLAS [10], only the $D_{13}(1900)$ assumption could be reconciled with the data, whereas the $P_{11}(1900)$ option could clearly be rejected [7]. In the $K^+\Sigma^0$ channel, four Δ^* states, $D_{33}(1700)$, $S_{31}(1900)$, $P_{31}(1910)$, and $P_{31}(1920)$, have been included (see Table II).

III. POLARIZATION FORMALISM

A. Polarization component definitions

The differential cross section for kaon electroproduction can be written as the product of a virtual photon flux factor Γ_v and the kaon virtual differential cross section, expressed in the kaon center-of-mass (c.m.) frame as

$$\frac{d\sigma}{d\Omega_{e'} d\Omega_K^{c.m.} dE_{e'}} = \Gamma_v \frac{d\sigma_v}{d\Omega_K^{c.m.}}. \tag{1}$$

The most general form for the differential cross section of a kaon from a proton target, allowing for a polarized electron beam, target proton, and recoil hyperon, is given by [35]

$$\begin{aligned} \frac{d\sigma_v}{d\Omega_K^{c.m.}} &= \mathcal{K} \sum_{\alpha,\beta} S_\alpha S_\beta \Big[R_T^{\beta\alpha} + \epsilon R_L^{\beta\alpha} + c_+ ({}^c R_{LT}^{\beta\alpha} \cos\Phi + {}^s R_{LT}^{\beta\alpha} \sin\Phi) \\ &+ \epsilon ({}^c R_{TT}^{\beta\alpha} \cos 2\Phi + {}^s R_{TT}^{\beta\alpha} \sin 2\Phi) \\ &+ h c_- ({}^c R_{LT'}^{\beta\alpha} \cos\Phi + {}^s R_{LT'}^{\beta\alpha} \sin\Phi) + h c_0 R_{TT'}^{\beta\alpha} \Big]. \end{aligned} \tag{2}$$

The $R^{\beta\alpha}$ terms represent the response functions that account for the structure of the hadronic system and, in general, are functions of Q^2, W, and $\cos\theta_K^{c.m.}$ only. The superscripts α and β refer to the target and hyperon polarization axes, respectively, and the c and s superscripts indicate a cosine or sine dependence on the angle Φ, where Φ is the angle between the electron and hadron planes. Here ϵ is the transverse polarization of the virtual photon, h is the electron-beam helicity, and $\mathcal{K}$ is the ratio of the momentum of the kaon to the virtual photon in the c.m. frame. The factors $c_\pm$ are given by $\sqrt{\epsilon(1 \pm \epsilon)}$ and $c_0 = \sqrt{1 - \epsilon^2}$. Fig. 2 defines the angles of the scattering process in the c.m. system.

The operators S_α and S_β project out the target polarization vector in the (x, y, z) system and the hyperon polar-

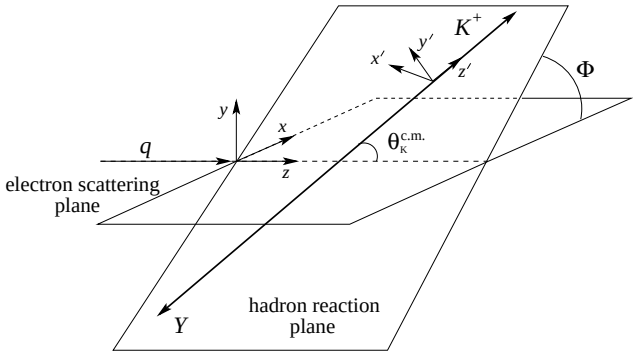

FIG. 2: Kinematics for KY electroproduction defining the c.m. angles and coordinate systems used in the analysis. This figure shows a positive Φ angle.

ization in the (x', y', z') system, respectively (see Fig. 2). The (x, y, z) system is defined such that $\hat{z}$ is along the three momentum transfer $\vec{q}$ direction and $\hat{y}$ is normal to the electron-scattering plane. The (x', y', z') system is defined such that $\hat{z}'$ is along the kaon momentum vector and $\hat{y}'$ is normal to the hadronic plane.

In the case where there is no beam, target, or recoil polarization (h, α, $\beta = 0$), Eq.(2) reduces to

$$\frac{d\sigma_v}{d\Omega_K^{c.m.}} \equiv \sigma_0 = \mathcal{K}\left[R_T^{00} + \epsilon R_L^{00} + c_+ R_{LT}^{00}\cos\Phi + \epsilon R_{TT}^{00}\cos 2\Phi\right]. \tag{3}$$

For the case of a polarized-electron beam incident on an unpolarized target producing a polarized recoiling hyperon, Eq.(2) becomes [36]

$$\frac{d\sigma_v}{d\Omega_K^{c.m.}} = \sigma_0(1 + hA_{LT'} + P_{x'}\hat{x}'\cdot\hat{S}_{x'} + P_{y'}\hat{y}'\cdot\hat{S}_{y'} + P_{z'}\hat{z}'\cdot\hat{S}_{z'}), \tag{4}$$

where $A_{LT'} = \frac{\mathcal{K}}{\sigma_0} c_- R_{LT'}^{00}\sin\Phi$ is the polarized beam asymmetry defined in terms of the fifth response function $R_{LT'}^{00}$.

Each of the recoil-hyperon polarization components can be split into a beam-helicity-independent part P_i^0, called the *recoil* polarization, and a beam-helicity-dependent part P_i', called the *transferred* polarization. The components of the hyperon polarization vector can be written as $P_i = P_i^0 + hP_i'$. The three recoil polarization components are given in terms of the response functions in the (x', y', z') system as

$$\begin{aligned}
P_{x'}^0 &= \frac{\mathcal{K}}{\sigma_0}\left(c_+ R_{LT}^{x'0}\sin\Phi + \epsilon\ R_{TT}^{x'0}\sin 2\Phi\right) \\
P_{y'}^0 &= \frac{\mathcal{K}}{\sigma_0}\left(R_T^{y'0} + \epsilon R_L^{y'0} + c_+ R_{LT}^{y'0}\cos\Phi + \epsilon R_{TT}^{y'0}\cos 2\Phi\right) \\
P_{z'}^0 &= \frac{\mathcal{K}}{\sigma_0}\left(c_+ R_{LT}^{z'0}\sin\Phi + \epsilon R_{TT}^{z'0}\sin 2\Phi\right),
\end{aligned} \tag{5}$$

and the three transferred polarization components are written in the (x', y', z') coordinate system as

$$\begin{aligned} P'_{x'} &= \frac{\mathcal{K}}{\sigma_0}\left(c_- R^{x'0}_{LT'}\cos\Phi + c_0 R^{x'0}_{TT'}\right) \\ P'_{y'} &= \frac{\mathcal{K}}{\sigma_0} c_- R^{y'0}_{LT'}\sin\Phi \\ P'_{z'} &= \frac{\mathcal{K}}{\sigma_0}\left(c_- R^{z'0}_{LT'}\cos\Phi + R^{z'0}_{TT'}\right). \end{aligned} \tag{6}$$

To accommodate finite bin sizes and to improve statistics, our analysis sums over all Φ angles. The Φ-integrated polarization components (represented by the $\mathcal{P}$ symbol) in the (x', y', z') system are given in Table III. In performing the Φ integration, the polarization components $\mathcal{P}^0_{x'}$, $\mathcal{P}^0_{z'}$, and $\mathcal{P}'_{y'}$ are equal to zero. In Table III, the term $K_I = 1/(R^{00}_T + \epsilon R^{00}_L)$.

(x', y', z') Coordinate System			
$\mathcal{P}^0_{x'}$	0	$\mathcal{P}'_{x'}$	$K_I c_0 R^{x'0}_{TT'}$
$\mathcal{P}^0_{y'}$	$K_I(R^{y'0}_T + \epsilon R^{y'0}_L)$	$\mathcal{P}'_{y'}$	0
$\mathcal{P}^0_{z'}$	0	$\mathcal{P}'_{z'}$	$K_I c_0 R^{z'0}_{TT'}$
(x, y, z) Coordinate System			
$\mathcal{P}^0_x$	0	$\mathcal{P}'_x$	$\frac{1}{2}K_I c_-(R^{x'0}_{LT'}\cos\theta^{c.m.}_K - R^{y'0}_{LT'} + R^{z'0}_{LT'}\sin\theta^{c.m.}_K)$
$\mathcal{P}^0_y$	$\frac{1}{2}K_I c_+(R^{x'0}_{LT}\cos\theta^{c.m.}_K + R^{y'0}_{LT} + R^{z'0}_{LT}\sin\theta^{c.m.}_K)$	$\mathcal{P}'_y$	0
$\mathcal{P}^0_z$	0	$\mathcal{P}'_z$	$K_I c_0(-R^{x'0}_{TT'}\sin\theta^{c.m.}_K + R^{z'0}_{TT'}\cos\theta^{c.m.}_K)$

TABLE III: Polarization observables integrated over Φ in the two coordinate systems used in this work.

To define the polarization observables in the (x, y, z) coordinate system, shown in Fig. 2, the components defined for the (x', y', z') system in Eqs.(5) and (6) must undergo a simple transformation that involves a rotation of $\theta^{c.m.}_K$ about $\hat{y}'$, followed by a rotation of Φ about $\hat{z}'$. The Φ-integrated recoil and transferred polarization components in the (x, y, z) system are defined in Table III.

B. σ_L/σ_T ratio

The Λ polarization transfer data can be used to extract the ratio of the longitudinal-to-transverse structure functions $R_\sigma = \sigma_L/\sigma_T$ at $\cos\theta^{c.m.}_K = 1$. This ratio has been previously measured at $\cos\theta^{c.m.}_K = 1$ [24, 37] and for $\cos\theta^{c.m.}_K \neq 1$ [6] using the Rosenbluth separation technique. Our previously published polarization transfer results [10] taken at a beam energy of 2.567 GeV were used to extract R_σ at $\cos\theta^{c.m.}_K = 1$ for three points of W and Q^2 [23]. In a similar way, R_σ can be extracted from the 4.261 and 5.754 GeV CLAS data.

In parallel or anti-parallel kinematics ($\cos\theta_K^{c.m.} = \pm 1$), the z' and z components of the transferred polarization integrated over Φ (given in Table III) reduce to

$$\mathcal{P}'_{z'} = \pm\mathcal{P}'_z = \pm\frac{c_0 R_{TT'}^{z'0}}{R_T^{00} + \epsilon R_L^{00}} = \pm\frac{c_0 R_{TT'}^{z'0}}{\sigma_U/\mathcal{K}}, \tag{7}$$

where the plus (minus) sign is associated with the parallel (anti-parallel) kinematics case and $\sigma_U = \sigma_T + \epsilon\sigma_L$.

The response functions used to express the Φ-integrated components of $\mathcal{P}'_{z'}$ and $\mathcal{P}'_z$ (see Table III) can be written in terms of the Chew, Goldberger, Low, and Nambu (CGLN) amplitudes [38] as shown in Ref. [35]. For the case of $\theta_K^{c.m.} = 0°$, it can be shown that $R_{TT'}^{z'0} = R_T^{00}$, and Eq.(7) can be rewritten as

$$\mathcal{P}'_{z'} = \mathcal{P}'_z = \frac{c_0 R_T^{00}}{R_T^{00} + \epsilon R_L^{00}} = \frac{c_0\sigma_T}{\sigma_T + \epsilon\sigma_L}. \tag{8}$$

Inverting this form and rearranging, the ratio R_σ at $\cos\theta_K^{c.m.} = \pm 1$ can be written as

$$R_\sigma = \frac{\sigma_L}{\sigma_T} = \frac{1}{\epsilon}\left(\frac{c_0}{\mathcal{P}'_{z'}} - 1\right). \tag{9}$$

While the $\mathcal{P}'_{z'}$ and $\mathcal{P}'_z$ data presented here do not include data points at $\theta_K^{c.m.} = 0°$, an extrapolation to $\cos\theta_K^{c.m.} = \pm 1$ can be performed as shown in Section VII C.

IV. POLARIZATION EXTRACTION

A. Decay angular distributions

The Λ decays weakly into a pion and a nucleon with the decay nucleon constrained to move preferentially in the direction of the hyperon spin. In the Λ rest frame, the decay nucleon angular distribution is given by [39]

$$\frac{dN}{d\cos\theta_N^{RF}} = N(1 + \alpha_\Lambda P_\Lambda \cos\theta_N^{RF}), \tag{10}$$

where P_Λ is the Λ polarization and θ_N^{RF} is the angle between the polarization axis and the decay-nucleon momentum in the Λ rest frame. In this work we focus solely on the $\Lambda \to p\pi^-$ decay (B.R.=64%) and explicitly replace θ_N^{RF} with θ_p^{RF}. The Λ weak decay asymmetry parameter α_Λ has been measured to be 0.642±0.013 [5].

The Σ^0 decays into a γ and a Λ (branching ratio 100%). A Σ^0 with polarization P_Σ will yield a decay Λ that retains some of the polarization of its parent. As shown in Ref. [40], $P_\Lambda = -\frac{1}{3}P_\Sigma$ on average for the decay Λ in its rest frame. For the case of a final-state Σ^0, the Λ rest frame can be calculated only if four particles are detected in the final state. In addition to the detection of the electron, kaon, and decay proton, either the decay pion of the Λ or the decay γ from the Σ^0 must be detected. Due to the small CLAS acceptance for a four particle final state, only three final-state particles were detected. In Ref. [9] it has been shown that the polarization of the daughter Λ from the Σ^0 decay can be measured without boosting the detected proton to the reference frame of the Λ. The value of the effective weak decay asymmetry parameter was determined to be $\alpha_\Sigma = -0.164$, or in terms of the Λ weak decay constant, $\alpha_\Sigma = -0.256\alpha_\Lambda$, thus reduced from the value $-0.333\alpha_\Lambda$. This value is independent of Σ^0 kinematics.

As the electron beam is not 100% polarized, the helicity term h in the hyperon polarization must be replaced by the average longitudinal electron-beam polarization P_b as

$$P_Y = P_Y^0 + P_b P_Y'. \tag{11}$$

Combining the expressions from Eqs.(10) and (11), the decay proton angular distribution for the two different beam helicity states can be written

$$\frac{dN^\pm}{d\cos\theta_p^{RF}} = N^\pm[1 + \alpha(P_Y^0 \pm P_b P_Y')\cos\theta_p^{RF}], \tag{12}$$

where $\alpha_\Lambda = 0.642$ for the Λ analysis and $\alpha_\Sigma = -0.164$ for the Σ^0 analysis.

B. Asymmetry approach

The transferred hyperon polarization was extracted using the acceptance-corrected yield asymmetry for the two different electron beam helicity states of the form

$$A = \frac{N^+ - N^-}{N^+ + N^-}. \tag{13}$$

This asymmetry is formed from the $\cos\theta_p^{RF}$ yields for the three spin-quantization axes of the decaying hyperon (in either of the coordinate systems defined in Fig. 2). The terms N^+ and N^- represent the acceptance-corrected decay

proton yields in a given kinematic bin. The helicity-gated yields are given by

$$N^{\pm}(\cos\theta_p^{RF}) = \mathcal{E}\left(\frac{d\sigma}{d\Omega}\right)^{\pm} = \sigma_0\mathcal{E}[1 \pm P_b A_{LT'} + \alpha(P_Y^0 \pm P_b P_Y')\cos\theta_p^{RF}], \tag{14}$$

where $\mathcal{E}$ represents the CLAS detection efficiency, which is assumed to be a helicity-independent function, and includes the CLAS acceptance function and the beam-target luminosity factors.

As discussed in Section III, this analysis was performed by integrating the decay proton yields over all Φ angles to maximize the statistical precision of the measurement. In this case the measured yield asymmetry becomes

$$A = \frac{\int_0^{2\pi}\sigma_0\mathcal{E}[1 + P_b A_{LT'} + \alpha(P_Y^0 + P_b P_Y')\cos\theta_p^{RF}]d\Phi - \int_0^{2\pi}\sigma_0\mathcal{E}[1 - P_b A_{LT'} + \alpha(P_Y^0 - P_b P_Y')\cos\theta_p^{RF}]d\Phi}{\int_0^{2\pi}\sigma_0\mathcal{E}[1 + P_b A_{LT'} + \alpha(P_Y^0 + P_b P_Y')\cos\theta_p^{RF}]d\Phi + \int_0^{2\pi}\sigma_0\mathcal{E}[1 - P_b A_{LT'} + \alpha(P_Y^0 - P_b P_Y')\cos\theta_p^{RF}]d\Phi}. \tag{15}$$

After some simplification, this expression can be written as

$$A = \frac{\int_0^{2\pi}\sigma_0[P_b A_{LT'} + \alpha P_b P_Y'\cos\theta_p^{RF}]d\Phi}{\int_0^{2\pi}\sigma_0[1 + \alpha P_Y^0\cos\theta_p^{RF}]d\Phi}. \tag{16}$$

As the $A_{LT'}$ term is proportional to $\sin\Phi/\sigma_0$, it integrates to zero for all choices of spin-quantization axes. Similarly, the term containing P_Y^0 integrates to zero along the (x, x') and (z, z') axes using the definitions in Section III.

Considering our coordinate system choices (see Fig. 2), it turns out that the Φ-integrated asymmetries can only be non-zero along the (x, x') and (z, z') axes. This can be seen as $\int_0^{2\pi}\sigma_0 P_Y' d\Phi = 0$ along both the (y, y') axes, given the polarization definitions in Section III. In other words, when performing the Φ integration, the polarization components $\mathcal{P}^0_{(z,z')}$, $\mathcal{P}^0_{(x,x')}$, and $\mathcal{P}'_{(y,y')}$ are all constrained to be zero. Thus the only possible non-zero asymmetries for our coordinate systems will be $A_{(z,z')}$ and $A_{(x,x')}$. Along these special axes, the Φ-integrated asymmetries can be written as

$$A = \alpha P_b\left[\frac{\int_0^{2\pi}\sigma_0 P_Y' d\Phi}{\int_0^{2\pi}\sigma_0 d\Phi}\right]\cos\theta_p^{RF}. \tag{17}$$

The quantity in brackets is equivalent to the $\mathcal{P}$ polarization terms in Table III and represents the Φ-integrated hyperon transferred polarization, where a separate asymmetry is computed for each spin-quantization axis. We therefore extract the non-zero transferred hyperon polarizations with respect to the different quantization axes from

the asymmetries by fitting

$$A_\Lambda = \alpha_\Lambda P_b \mathcal{P}'_\Lambda \cos\theta_p^{RF} \quad \text{or} \quad A_\Sigma = \alpha_\Sigma P_b \mathcal{P}'_\Sigma \cos\theta_p^{RF}. \tag{18}$$

In forming the asymmetry of Eq.(13), the decay proton helicity-gated yields are sorted for each kinematic bin of interest. We used an event-by-event weighting factor to correct the yields for the detector acceptance. The asymmetry method used in this analysis is relatively insensitive to the detailed form of the CLAS acceptance function. This discussion is contained in Section V D.

C. Hyperon polarization and statistical uncertainty

For the general case where a given hyperon sample Y is contaminated by particle misidentification events and events from the tail of the hyperon Y', the helicity asymmetry can be written in terms of its individual contributions as

$$\begin{aligned} A_{meas} &= \frac{(N_Y^+ + N_{Y'}^+ + N_{bck}^+) - (N_Y^- + N_{Y'}^- + N_{bck}^-)}{N_Y + N_{Y'} + N_{bck}} \\ &= \frac{\frac{N_Y^+ - N_Y^-}{N_Y} + \frac{N_{Y'}^+ - N_{Y'}^-}{N_{Y'}} \cdot \frac{N_{Y'}}{N_Y} + \frac{N_{bck}^+ - N_{bck}^-}{N_{bck}} \cdot \frac{N_{bck}}{N_Y}}{1 + \frac{N_{Y'}}{N_Y} + \frac{N_{bck}}{N_Y}}, \end{aligned} \tag{19}$$

where N_Y, $N_{Y'}$, and N_{bck} refer to the number of counts from the hyperon of interest, the tail of the other hyperon, and from the background (mostly pions misidentified as kaons), respectively, within the Y identification cuts (see Section V E). If we define $F_{Y'} = N_{Y'}/N_Y$ and $F_{bck} = N_{bck}/N_Y$, we can write

$$A_{meas} = \frac{A_Y + A_{Y'} F_{Y'} + A_{bck} F_{bck}}{1 + F_{Y'} + F_{bck}}. \tag{20}$$

It was observed in this analysis that the pion background asymmetry under both hyperon peaks is consistent with zero, thus the term associated with A_{bck} in Eq.(20) is set to zero (see Section V F). The "pure" asymmetries, A_Λ and A_Σ, are given by Eq.(18), thus the measured asymmetry can be written in terms of the transferred polarizations, as well as the measured polarization within the hyperon mass cuts $\mathcal{P}'_{meas}$ as

$$A_{meas} = \frac{\alpha_Y P_b \mathcal{P}'_Y \cos\theta_p^{RF} + \alpha_{Y'} P_b \mathcal{P}'_{Y'} \cos\theta_p^{RF} F_{Y'}}{1 + F_{Y'} + F_{bck}} = \alpha_\Lambda P_b \mathcal{P}'_{meas} \cos\theta_p^{RF}, \tag{21}$$

where $\alpha_\Lambda P_b \mathcal{P}'_{meas}$ is the slope extracted from the fit of the $\cos\theta_p^{RF}$ distribution with respect to a given spin-quantization axis.

We found that the contamination of Σ^0 hyperons within the Λ identification cuts is consistent with zero (see Section V E), so for $Y = \Lambda$ and $Y' = \Sigma^0$, Eq.(21) can be rearranged to get

$$\mathcal{P}'_\Lambda = \mathcal{P}'_{meas}(1 + F_{bck}). \tag{22}$$

For $Y = \Sigma^0$ and $Y' = \Lambda$, Eq.(21) can be rearranged to get

$$\mathcal{P}'_\Sigma = \frac{\alpha_\Lambda}{\alpha_\Sigma}\left[\mathcal{P}'_{meas}(1 + F_\Lambda + F_{bck}) - \mathcal{P}'_\Lambda F_\Lambda\right]. \tag{23}$$

Performing standard error propagation, the statistical uncertainty for $\mathcal{P}'_\Lambda$ is

$$\delta\mathcal{P}'_\Lambda = \left[(1 + F_{bck})(\delta\mathcal{P}'_{meas})^2 + (\mathcal{P}'_{meas})^2\delta F_{bck}^2\right]^{1/2}, \tag{24}$$

where the individual uncertainties are given by

$$\delta F_{bck} = F_{bck}\sqrt{\frac{1}{N_{bck}} + \frac{1}{N_\Lambda}} \quad \text{and} \quad \delta\mathcal{P}'_{meas} = \frac{\delta(\text{slope})}{\alpha_\Lambda P_b}. \tag{25}$$

Here δ(slope) is the uncertainty in the slope from the fit of the $\cos\theta_p^{RF}$ distribution. We find that the dominant contribution to the Λ polarization uncertainty is due to the uncertainty in $\mathcal{P}'_{meas}$.

Similarly, the statistical uncertainty for $\mathcal{P}'_\Sigma$ is

$$\delta\mathcal{P}'_\Sigma = \frac{\alpha_\Lambda}{\alpha_\Sigma}\left[(1 + F_\Lambda + F_{bck})^2(\delta\mathcal{P}'_{meas})^2 + (\mathcal{P}'_{meas} - \mathcal{P}'_\Lambda)^2\delta F_\Lambda^2 + (\mathcal{P}'_{meas}\delta F_{bck})^2 + (F_\Lambda\delta\mathcal{P}'_\Lambda)^2\right]^{1/2}, \tag{26}$$

where the individual uncertainties are given by

$$\delta F_\Lambda = F_\Lambda\sqrt{\frac{1}{N_\Lambda} + \frac{1}{N_\Sigma}}, \tag{27}$$

$$\delta F_{bck} = F_{bck}\sqrt{\frac{1}{N_{bck}} + \frac{1}{N_\Sigma}}, \quad \text{and} \tag{28}$$

$$\delta\mathcal{P}'_{meas} = \frac{\delta(\text{slope})}{\alpha_\Lambda P_b}. \tag{29}$$

The dominant contribution to the Σ^0 statistical uncertainty arises due to the uncertainty in $\mathcal{P}'_{meas}$. All other terms are at least a factor of 4 smaller in size.

D. Depolarization factor

Our formalism defines the polarization transfer as the ratio of the hyperon polarization to that of the electron beam. However, the electron interacts with the hadronic system through the exchange of a virtual photon. Thus the true "beam" polarization is given by the product $P_b D(y)$, where $D(y)$ accounts for the polarization loss from the incident beam electron to the virtual photon. There are a number of ways to express the factor $D(y)$. One form is given by [41]

$$D(y) = \frac{y(2-y)}{2(1-y)(1+R_\sigma)+y^2}, \tag{30}$$

where $y = E_{\gamma^*}/E_b$ is the relative energy transfer to the target proton and $R_\sigma = \sigma_L/\sigma_T$.

With this accounting, the hyperon polarization can be rewritten from Eq.(11) as $P_Y = P_Y^0 + P_b D(y) P'_Y$. This would lead to slightly modified forms of the asymmetries in Eq.(18) with the hyperon polarizations scaled by a factor of $1/D(y)$. This re-expression of the hyperon transferred polarization allows for a more direct comparison for experiments performed at different beam energies. Perhaps, more importantly, it allows for a more direct comparison of electroproduction and photoproduction data sets where the "trivial" depolarization factor is accounted for in the electroproduction data.

Having made this distinction in the possible convention choice for the hyperon transferred polarization, we have decided not to account for it in this work, following instead the procedures in Ref. [10]. The main reason for this choice is to avoid introducing a model-dependent uncertainty into our quoted polarizations. Our studies have shown that with different hadrodynamic models, the variation in $D(y)$ due to variations in R_σ can be up to 20%.

Shown in Fig. 3 are predictions of the depolarization factor for several of our kinematic bins using the MB model [42]. It is seen that in our kinematics $\langle D(y) \rangle \sim 0.6$. The polarization transfer from the virtual photon to the hyperon is therefore 67% larger on average than that for the beam electron to the hyperon. When considering the polarization data in Section VII, one must take into account the depolarization factor when comparing to other data and to theory. The theory calculations shown in Section VII match the data, namely they show the product of the depolarization factor and the polarization.

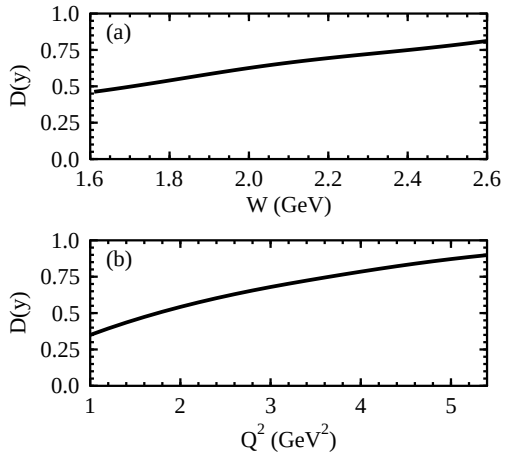

FIG. 3: Calculations of the depolarization factor $D(y)$ at 5.754 GeV using the MB model [42] in representative data sorts (a) summing over all Q^2 and $\cos\theta_K^{c.m.}$ and (b) summing over all W and $\cos\theta_K^{c.m.}$.

V. DATA ANALYSIS

A. The CLAS detector

All of the data shown in this analysis were collected using the CLAS spectrometer located in Hall B at JLab [43]. The main magnetic field of CLAS is provided by six superconducting coils, which produce an approximately toroidal field in the azimuthal direction around the beam axis. The gaps between the cryostats are instrumented with six identical detector packages, as shown in Fig. 4. Each sector consists of three sets of drift chamber (DC) packages [44] to determine the trajectories of the charged particles, Cherenkov counters (CC) [45] for electron identification, scintillator counters (SC) [46] for charged particle identification, and electromagnetic calorimeters (EC) [47] for electron identification and detection of neutral particles. A 5-cm long liquid-hydrogen target was located in the center of the detector on the electron beam axis.

To reduce the electromagnetic background resulting from Møller scattering off atomic electrons in the target and the target cell, a small normal-conducting toroidal magnet (called the mini-torus) was placed symmetrically about the target inside of the first DC package. This magnetic field sweeps Møller electrons out of the detector volume. A totally absorbing Faraday cup, located at the end of the beam line, was used to determine the integrated beam charge passing through the target. The efficiency of detection and reconstruction for stable charged particles in the fiducial regions of CLAS is greater than 95%. The solid angle coverage of CLAS is approximately 3π sr. The polar angle coverage for electrons ranges from 8° to 45°, while for hadrons it is from 8° to 142°, with an angular resolution of $\delta\theta, \delta\phi \sim 1$ of better than 2 mr. The CLAS detector was designed to track particles having momenta greater than roughly 200 MeV with a resolution $\delta p/p$ in the range of 0.5 to 1%.

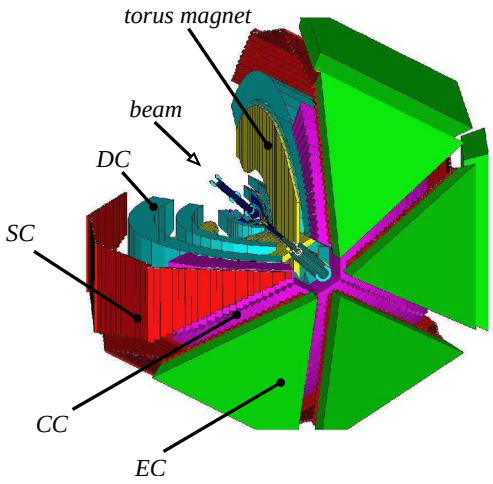

FIG. 4: (Color online) Three dimensional view of the CLAS detector with the different subsystems labeled. A single sector of the detector has been cut away to enable a view of the inner subsystems. The diameter of the CLAS detector is ∼5 m and it is ∼8 m long.

The large acceptance of CLAS enabled us to detect the final-state electron and kaon, as well as the proton from the decay of the Λ hyperon. Hyperon identification with CLAS relies on missing-mass reconstructions of the reaction $e + p \rightarrow e' + K^+ + X$. In this section, details are provided on our procedures for particle identification, the cuts used to isolate the $K^+\Lambda$ and $K^+\Sigma^0$ final states, the hyperon spectrum fitting procedures, and other cuts and corrections.

B. Data set information

The data were taken with typical electron beam currents of 5 nA at a luminosity of 1×10^{34} cm^{-2}s^{-1}. The CLAS event readout was triggered by a coincidence between a Cherenkov counter and a calorimeter detector in a single sector, generating an event rate of ∼2 kHz. The main CLAS torus had its polarity set such that negatively charged particles were bent toward the electron beam line. The electron beam was longitudinally polarized, with the polarization determined by a coincidence Møller polarimeter. Beam polarization measurements were taken at regular intervals throughout the running periods and measured a stable electron beam polarization of 70%.

The data in this paper were collected as part of the CLAS running periods `e1c` in early 1999 and `e1-6` in late 2001/early 2002. The `e1c` running period included data with beam energies of 2.567 GeV (previously published in Ref. [10]) and 4.261 GeV acquired at several different field settings of the main CLAS torus. 4.261 GeV represents the luminosity-averaged beam energy for data taken with electron beam energies of 4.056, 4.247, and 4.462 GeV. Combining the data sets is justified given the relatively small spread in the virtual photon polarization parameter ϵ among the different energies. The `e1-6` running period was taken with an electron beam energy of 5.754 GeV.

Information regarding the different run periods, including the total number of triggers, the approximate W and Q^2 ranges of the data, the number of hyperons in the different analyses detected through the $e'K^+p$ final state, and the average beam polarization, is contained in Table IV.

E_b	Triggers	W	Q^2	N_Λ	N_{Σ^0}	$\langle P_b \rangle$
2.567 GeV	910 M	1.6 – 2.15 GeV	0.3 – 1.5 GeV^2	42000	8000	67%
4.261 GeV	1599 M	1.6 – 2.6 GeV	0.7 – 3.5 GeV^2	34000	6500	67%
5.754 GeV	5083 M	1.6 – 2.6 GeV	1.3 – 5.4 GeV^2	82000	16000	72%

TABLE IV: Information regarding the different CLAS electroproduction data sets associated with this work, including the number of raw triggers, the W and Q^2 extents of each data set, the number of hyperons (detected via the $e'K^+p$ final state), and the average longitudinal polarization of the electron beam. Note that the 4.261 GeV data set sums together data acquired at beam energies of 4.056, 4.247, and 4.462 GeV.

C. Particle identification

The first level of event reconstruction required the identification of a viable electron candidate. This was done by requiring that a negatively charged particle – identified by its track curvature in the magnetic field of the spectrometer – be matched in time and space with hits in the SC, CC, and EC counters. A particle-tracking vertex cut was employed to ensure that the particle originated from the liquid-hydrogen target. In order to remove negatively charged pions from the electron candidate sample, a cut was placed on the ratio of the measured energy deposited in the fiducial region of the EC (accounting for the sampling fraction of the calorimeter) to the momentum of the particle. A further reduction in pion contamination was achieved by placing a minimum-ionizing cut on the energy measured in the EC.

The first-level requirements for charged hadrons are that they have a track in the drift chamber and a matched, in-time hit in the SC in that same sector. For the final-state K^+ and p in this analysis, we require that the curvature for the K^+ and p tracks be consistent with a positively charged particle. We also require that the K^+ track originate from the target using a vertex cut.

The algorithm used for hadron identification was slightly different between the `e1c` and `e1-6` data sets. For the `e1c` data set, the final-state particles were identified with momentum-dependent cuts on the momentum vs. mass distribution (to account for the worsening resolution of CLAS with increasing momentum). For the `e1-6` analysis, hadron identification was performed using a timing cut. The timing quantity of interest ($\delta t = t_1 - t_2$) was the difference in the time between the measured flight time for a particle from the event vertex to the SC system (t_1) and that expected for a given hadron type (t_2). The quantity t_2 was computed for all positively charged particles assuming the mass of the pion, kaon, and proton. A small δt indicates that the correct mass hypothesis has been

made. The timing cuts are defined such that only one mass hypothesis can be satisfied for a given hadron. Fig. 5 shows the δt plots used to identify final-state π^+, K^+, and p candidates.

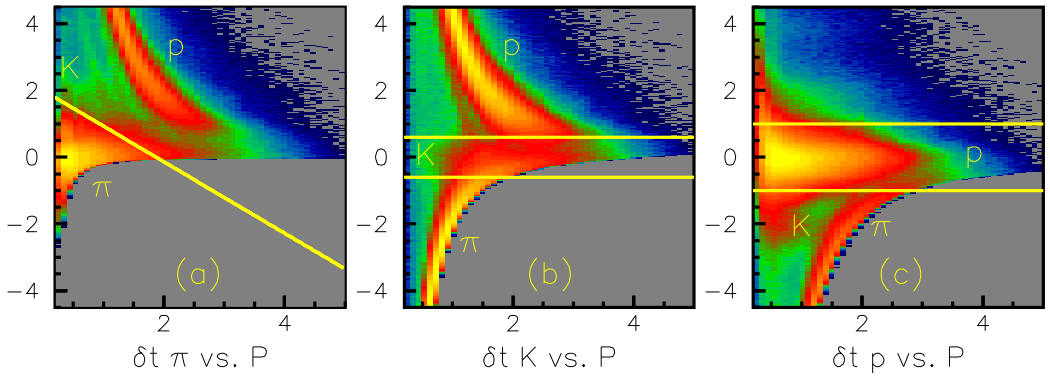

FIG. 5: Time difference δt (ns) between the SC system and the flight time calculated for specific hadron-mass hypotheses plotted against the hadron momentum P (GeV) for (a) π^+, (b) K^+, and (c) p at 5.754 GeV. Each plot shows the timing cuts imposed upon the spectra for the given mass hypothesis.

Prior to imposition of final particle identification cuts and in order to ensure an optimal resolution for the hyperon missing mass spectrum, the reconstructed momenta for the electrons and charged hadrons in the final state were corrected for small imperfections in the torus magnetic field map and the drift chamber alignment by using reactions with over-determined kinematics. The size of the momentum corrections ($\delta p/p$) for each of the final-state particles is on the order of 1%.

D. Acceptance corrections

In order to correct the yields for the detector acceptance, it is necessary to employ cuts that define the regions of CLAS where the detection efficiency is reasonably large and uniform. These fiducial cuts for both electrons and positive hadrons depend on momentum, angle, and torus field setting. For the electron, the CLAS acceptance is determined mostly by the limits of the azimuthal angle ϕ_e acceptance in each sector. The ϕ_e limits are determined by a marked drop in the collection efficiency of the CC at the edges of the detector. Additional fiducial cuts for all charged particles are designed to exclude regions of non-uniform acceptance from attenuation due to interactions with the mini-torus coils, the torus cryostat, or from the edges of the drift chamber acceptance.

The acceptance correction was based on an analytic calculation that determined the geometrical acceptance factor on an event-by-event basis given the ϕ acceptance of each final-state particle within the defined geometrical fiducial region. This factor accounted for losses due to kaon decays in-flight, bad scintillator paddles in the SC system, and the $\Lambda \to p\pi^-$ branching ratio. Typical acceptances for the KY reactions requiring detection of the $e'K^+p$ final state

are at the level of 5% to 20%. A detailed comparison between the nominal geometric acceptance correction and a full GEANT acceptance function was performed for the `e1c` analysis (see Ref. [48]). Both methods were shown to have very similar functional forms. However, the beauty of the asymmetry approach employed for this analysis is that the results are relatively insensitive to the acceptance correction. Thus a much simpler analytic form was chosen over a full Monte Carlo approach.

E. Hyperon yield extraction

The reactions of interest are identified from missing-mass (MM) reconstructions of the $e'K^+$ final state. Shown in Fig. 6(a) is the $MM(e'K^+)$ distribution for the $e'K^+p$ final state at 5.754 GeV. This spectrum shows substantial, well-separated peaks for the ground state Λ and Σ^0 hyperons. The width of the Λ peak in this spectrum, summed over all Q^2 and W, is about 11 MeV. Fig. 6(b) shows the $MM^2(e'K^+p)$ (missing mass squared) distribution. Here the final-state proton can come from the decay of the $\Lambda(1115)$ (missing π^-), the $\Sigma^0(1192)$ (missing $\pi^-\gamma$), or the $\Lambda(1520)$ (missing K^-). Fig. 6(a) requires a cut on the $MM^2(e'K^+p)$ spectrum in the range from 0.007 to 0.065 GeV^2, as shown in the correlation plot of Fig. 6(c), to reduce the contributions of particle misidentification background. The final $K^+\Lambda$ and $K^+\Sigma^0$ yields are then extracted through the fitting procedures described below.

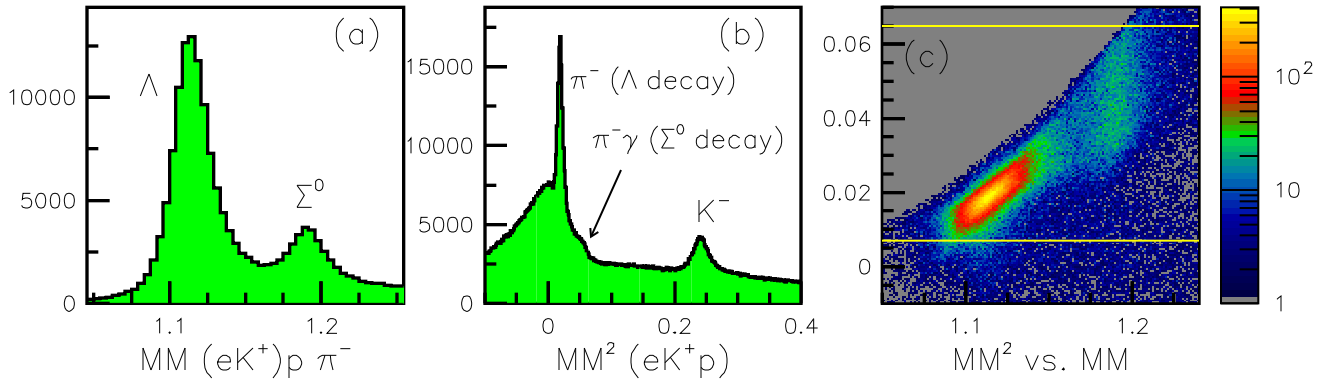

FIG. 6: (Color online) $e'K^+p$ final state data from runs at 5.754 GeV. (a) Missing mass for $p(e,e'K^+)X$. (b) Missing mass squared for $p(e,e'K^+p)X$. (c) $MM^2(e'K^+p)$ vs. $MM(e'K^+)$ showing the cuts used to select the $K^+\Lambda$ and $K^+\Sigma^0$ event samples. (Units in GeV.)

The three components to the hyperon missing mass spectrum are the $K^+\Lambda$ final-state events, the $K^+\Sigma^0$ final-state events, and the particle-misidentification background (dominated by pions misidentified as kaons). As discussed in Section IV, these individual contributions must be determined to extract the Λ and Σ^0 polarizations, and they have been measured through fits to the hyperon mass distributions. In this procedure, the Λ and Σ^0 peaks were fit using templates derived from a phase-space GEANT Monte Carlo simulation. The templates were generated with radiative

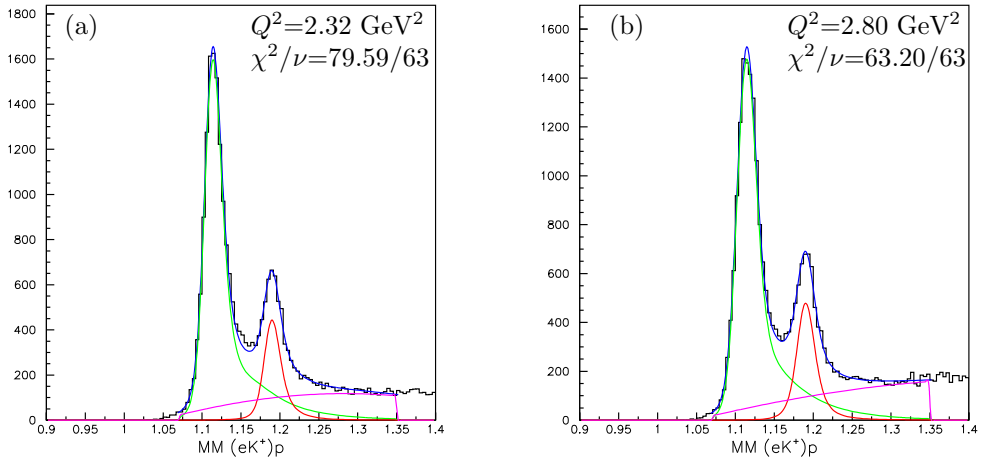

FIG. 7: (Color online) Sample hyperon spectrum fit results using hyperon templates derived from Monte Carlo (Λ:green curve, Σ^0:red curve) and a third-order polynomial for the background (magenta curve). The smoothed templates have been allowed to shift along the mass axis and convoluted with a Gaussian to give the best χ^2 per degree of freedom (χ^2_ν) values for the fits. These distributions at 5.754 GeV are summed over all W and $\cos\theta_K^{c.m.}$ for central Q^2 values as indicated. The blue curve shows the full fit result.

effects turned on, which is necessary to account for the Λ radiative tail beneath the Σ^0 peak. The background contributions in each bin were studied employing two different procedures. In the first, a background spectrum was derived from Monte Carlo using a phase space generator for multi-pion final states. The final-state π^+ were then assigned the K^+ mass. The resultant $MM(e'\pi^+)$ spectra were then sorted into the different analysis bins in Q^2, W, and $\cos\theta_K^{c.m.}$. The second approach employed a third-order polynomial to fit the backgrounds in the spectra. These two models for the background gave consistent answers, however the polynomial model was employed for the final fits as the Monte Carlo background distributions were statistically limited.

The form of the hyperon spectrum fit in each analysis bin was given by

$$MM = A \cdot \Lambda_{template} + B \cdot \Sigma_{template} + P(3)_{bck}, \tag{31}$$

where $\Lambda_{template}$ and $\Sigma_{template}$ are the simulated hyperon distributions with weighting factors A and B, respectively, and $P(3)_{bck}$ is a third-order polynomial describing the background. In performing these fits, the Λ and Σ^0 Monte Carlo templates were allowed to shift up to $\pm$10 MeV to match the data. In addition, the hyperon templates were individually convoluted with a Gaussian with a width chosen to minimize the χ^2 of the fits in each bin. This was necessary as the resolution of the Monte Carlo was not a perfect match to the real data. Finally, the Monte Carlo templates were smoothed using a spline fit to remove the effects of statistical fluctuations in the simulation samples. Fits for two representative bins are shown in Fig. 7.

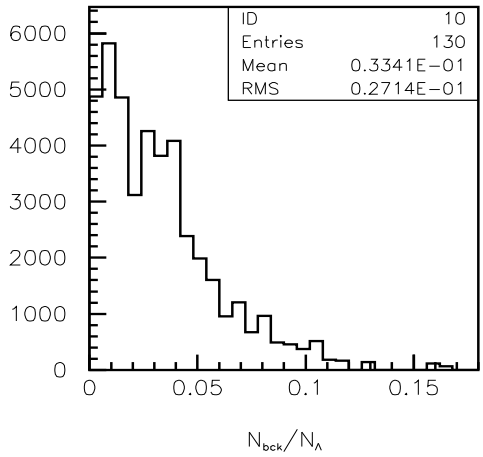

FIG. 8: Ratio of the number of background counts to Λ counts in the Λ analysis mass window weighted by the uncertainty in the ratio for each of the kinematic bins in this analysis at 5.754 GeV.

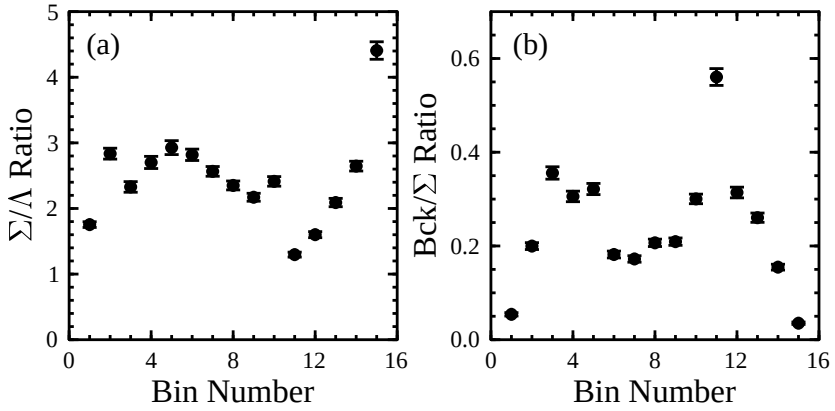

FIG. 9: Ratios of the number of counts in the Σ^0 analysis mass window for the data at 5.754 GeV. (a) Σ^0/Λ ratio. (b) Background/Σ^0 ratio.

Fig. 8 shows the results of the yield fits in terms of $F_{bck} = N_{bck}/N_\Lambda$ for events in our Λ mass window ($MM(e'K^+)$ from 1.080 to 1.160 GeV) for each of our data sorts. The plot shows the distribution of the background ratio for each bin weighted by the uncertainty in the ratio. As the particle misidentification background was found to be relatively independent of kinematics, a single value of F_{bck}=3.3% has been employed for all analysis bins based on the weighted mean of Fig. 8. Additionally, from the spectrum fits we have extracted the ratios $F_{Y'} = N_{\Sigma^0}/N_\Lambda$ and $F_{bck} = N_{bck}/N_{\Sigma^0}$ in our Σ^0 mass window ($MM(e'K^+)$ from 1.175 to 1.213 GeV) (see Fig. 9). These ratios are relatively independent of the kinematics. However, due to the sensitivity of $\mathcal{P}'_\Sigma$ to the number of Λ events in the Σ^0 mass window, we have employed the measured Σ^0, Λ, and background yields in the Σ^0 analysis for each kinematic bin.

F. Background polarization corrections

Once the number of Λ, Σ^0, and background events are determined in each of the respective hyperon mass windows, the measured polarization must be corrected as discussed in Sec. IV C. The background polarization was measured by sorting data from the $ep \to e'\pi^+pX$ reaction and assigning the K^+ mass to the π^+ events. The analysis procedure then followed all of the same steps and procedures as for the hyperon polarization analysis. The measured background polarization for one typical data sort is shown in Fig. 10 as a function of W (summed over all other kinematic variables). The results are consistent with $\mathcal{P}'_{bck}$=0 for all axes in all of the sorts investigated.

Within the tight Λ cuts, there was no measurable level of Σ^0 contamination. However, within the Σ^0 mass window (1.175 to 1.213 GeV) there is significant contamination from both the Λ radiative tail and pion background (see Table V). To correct the Σ^0 polarization for the Λ tail, $\mathcal{P}'_\Lambda$ was determined following our nominal prescription for determining the transferred Λ polarization, where the Λ data were binned in the same bins as the Σ^0 data. This value of $\mathcal{P}'_\Lambda$ was then used in Eq.(23) to calculate the corrected Σ^0 polarization.

W Bin (GeV)	N_Σ	N_Λ	N_π
1.825	3067±79	2746±20	92±27
1.975	3872±85	2544±22	214±28
2.125	2425±72	2074±20	329±24
2.275	3160±80	2050±20	501±26
2.470	3413±80	1758±19	408±19

TABLE V: Results from the 5.754 GeV yield fits for N_Σ, N_Λ, and N_{bck} with statistical uncertainties in a $\pm 2\sigma$ Σ^0 mass window for a sort dividing the Σ^0 analysis into 5 bins in W.

G. Radiative corrections

No radiative corrections have been applied to the data in this analysis. These have purposefully been avoided by employing relatively tight cuts on the reconstructed hyperon spectrum for the $K^+\Lambda$ and $K^+\Sigma^0$ events and by accounting for the $K^+\Lambda$ radiative tail events within the $K^+\Sigma^0$ event sample. This is expected to be a reasonable approach as the radiative effects are independent of the beam helicity and thus should effectively cancel out of the asymmetry calculation. With our relatively tight hyperon mass cuts, the maximum radiated photon energy is only about 50 MeV, which has a negligible impact on our computed $\cos\theta_p^{RF}$ values with respect to each quantization axis.

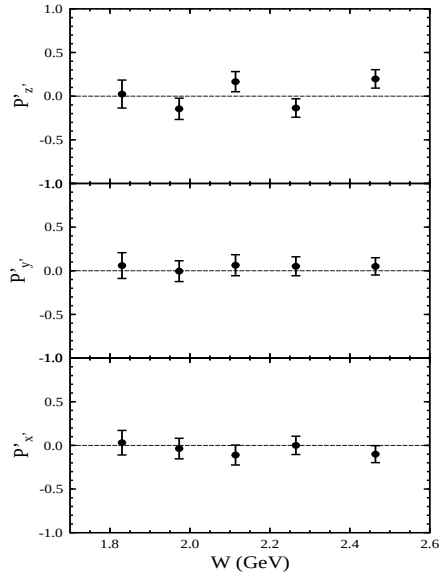

FIG. 10: Polarization $\mathcal{P}'$ vs. W for the pion misidentification background in the (x', y', z') coordinate system for the data summed over all Q^2 and $d\Omega_K^{c.m.}$.

H. Bin averaging corrections

The bin sizes for W, Q^2, and $\cos\theta_K^{c.m.}$ in this analysis were chosen to roughly equalize the statistical precision of each polarization data point. To account for the finite bin sizes and the variation of the cross section over the bins, we quote our polarization results at the bin means. The bin mean was determined by measuring the mean of the acceptance-corrected yield distribution over the kinematic bins of interest. As might be expected, the largest differences between the bin mean and the bin center occur where the bins are larger. The kinematic bin means for each data sort are given in Section VII.

VI. SYSTEMATIC UNCERTAINTY ANALYSIS

In this section we examine the sources of systematic uncertainty that affect the extracted polarization observables for the 5.754 GeV data set. The assigned systematics for the 4.261 GeV $K^+\Lambda$ data set are described in Ref. [49] and are given by $\delta\mathcal{P}'_{sys} < 0.084$. The contributions to the total systematic uncertainty belong to one of four general categories: Polarization extraction, beam-related factors, acceptance function, and background contributions. As the statistics for the $K^+\Lambda$ final state dominate those for the $K^+\Sigma^0$ final state, the determination of the assigned systematics for both final states is based on analysis of the $K^+\Lambda$ data. The exception to this is the assignment of a separate systematic for the background contributions. The final systematic uncertainty compilation for the 5.754 GeV measurements is given in Table VI.

The procedure used to assign a systematic uncertainty to each source within a given category is to compare the measured polarization $\mathcal{P}'$ for all kinematic bins with the nominal analysis cuts or procedures (*nom*) to that with modified cuts or procedures (*mod*). The spread in the difference of the polarization over all data points, $\Delta\mathcal{P}' = \mathcal{P}'_{nom} - \mathcal{P}'_{mod}$, is used as a measure of the systematic uncertainty for a given source. The estimated common uncertainty for a given source is the weighted root-mean-square (r.m.s.) of $\Delta\mathcal{P}'$ for all points given by

$$\delta\mathcal{P}'_{sys} = \sqrt{\frac{\sum_{i=1}^{N}(\Delta\mathcal{P}'_i)^2/(\delta\mathcal{P}'_i)^2}{\sum_{i=1}^{N}1/(\delta\mathcal{P}'_i)^2}}, \tag{32}$$

where the sums are over all N data points and $\delta\mathcal{P}'_i$ is the statistical uncertainty of the i^{th} data point. In the studies done for this analysis, a common systematic uncertainty is applied for all data points as the kinematic dependence of the $\Delta\mathcal{P}'$ distributions was found to be minimal. In each of the systematic uncertainty studies performed for this analysis, the widths of the $\Delta\mathcal{P}'$ distributions were much larger than the measured centroids, which are all consistent with zero. Thus the assignments are believed to be rather conservative.

A. Polarization extraction

The polarization has been determined by using two different analysis approaches. The nominal technique is the asymmetry approach described in Section IV. An alternative approach is to extract the polarization from the ratio of the acceptance-corrected, helicity-gated yields via

$$R = \frac{\sigma^+}{\sigma^-} = \frac{1 + \alpha_\Lambda P_b \mathcal{P}'_\Lambda \cos\theta_p^{RF}}{1 - \alpha_\Lambda P_b \mathcal{P}'_\Lambda \cos\theta_p^{RF}}. \tag{33}$$

The difference between these two techniques resulted in an estimated systematic uncertainty of $\delta\mathcal{P}'_{sys} = 0.008$.

A systematic uncertainty arises from the somewhat arbitrary choice made for the $\cos\theta_p^{RF}$ bin size. Nominally the data were sorted into six bins in the rest frame proton angle. A comparison of the nominal polarization results with the extraction from a sort with four and eight bins in this variable resulted in a weighted r.m.s. of $\delta\mathcal{P}'_{sys} = 0.018$. The difference in the polarization results is effectively due to the fitting algorithm employed in which the centroids of the $\cos\theta_p^{RF}$ bins are assigned to the center of the bin. When the number of bins is reduced, the fit results are more sensitive to the bin content.

The final systematic uncertainty contribution in this category arises due to the uncertainty in the weak decay

asymmetry parameter α_Λ. This uncertainty gives rise to a scale-type uncertainty on the extracted polarization (the same for both Λ and Σ^0 hyperons) given by $\delta\mathcal{P}'_{sys} = |\mathcal{P}'_Y|\delta\alpha_\Lambda/\alpha_\Lambda = 0.02|\mathcal{P}'_Y|$.

B. Beam-related factors

There are two possible contributions to the systematic uncertainty related to the beam. The first factor is associated with the beam polarization measurement from the Møller polarimeter system. This arises from the uncertainty in the Møller target foil polarization, the statistical uncertainty in the measurements, as well as a contribution from variations of the polarization measurements over time. These contributions have been estimated for CLAS polarization measurements to be 4%. The associated uncertainty in the hyperon polarization is $\delta\mathcal{P}'_{sys} = |\mathcal{P}'_Y|\delta P_b/P_b = 0.04|\mathcal{P}'_Y|$.

The second beam-related contribution is the beam charge asymmetry that results from a difference in the electron beam intensity for the two beam helicity states. From studies of the 5.754 GeV data set, the beam charge asymmetry was below the 10^{-3} level and no detectable difference between the helicity-gated live times was found, thus no systematic contribution was assigned.

C. Acceptance function

There are several factors that go into the systematic uncertainty associated with the form of our acceptance correction and with the choices made to implement this correction, which include the specific form of the fiducial cuts used to define the azimuthal extent of the acceptance as a function of polar angle and the minimum acceptance cutoff. In order to assign a systematic uncertainty associated with the acceptance correction, we have compared the extracted polarizations with and without the geometric acceptance corrections. The r.m.s. width of the difference distribution was assigned as the systematic uncertainty for the acceptance correction. This value, $\delta\mathcal{P}'_{sys} = 0.033$, is believed to be a very conservative estimate.

To study the effects of the fiducial cuts employed to define the azimuthal acceptance for electrons and hadrons, two different sets of fiducial cuts were defined in the analysis. A loose cut (the nominal cut) was designed to define the azimuthal acceptance edge of CLAS as a function of momentum, and a second cut was designed to be several degrees tighter than the nominal cut. Comparisons of the extracted polarizations between these two cut definitions gave an r.m.s. width of $\delta\mathcal{P}'_{sys} = 0.020$, which represents the assigned systematic uncertainty.

The minimum acceptance cutoff translates into a maximum acceptance weight. The minimum acceptance cutoff

was nominally set at 10% (a somewhat arbitrary choice) for the $e'K^+p$ final state. For our study, we varied the acceptance cutoff by ±20% relative to the nominal cutoff value. The assigned systematic uncertainty, given by the r.m.s. width of the polarization difference distribution, is $\delta\mathcal{P}'_{sys} = 0.025$.

D. Background contributions

1. $e'K^+\Lambda$ final state

Our analysis of the backgrounds found no measurable level of Σ^0 contamination within our final $K^+\Lambda$ event sample. However, there is a few percent contamination of π^+ misidentification events that remain beneath the Λ peak that serve to dilute the measured Λ polarization. To estimate the systematic uncertainty associated with our subtraction technique, we have compared our nominal polarization results to results obtained assuming no pion background. Clearly, this would result in an overestimate of the systematic uncertainty so we have used one-half of the difference, or $\delta\mathcal{P}'_{sys} = 0.009$. While an arbitrary choice, this represents a conservative estimate and is small compared to other sources of systematic uncertainties.

2. $e'K^+\Sigma^0$ final state

The uncertainties in the backgrounds from $K^+\Lambda$ and pion misidentification have a much bigger impact on the extracted Σ^0 polarization compared to the Λ analysis. Therefore, it is important to study these effects separately for this final state. Our approach to assign a systematic uncertainty due to the fit uncertainties of the contributing backgrounds beneath the Σ^0 is to allow the extracted yields to vary by ±10% from the fit value and to study the effect on the extracted Σ^0 polarization. Variations of the background levels of ±10% amounted to variations on the fitted background yields of $N_\Lambda \pm 2\sigma_{N_\Lambda}$ and $N_{bck} \pm 2\sigma_{N_{bck}}$. Our studies indicated that the maximum change in the measured Σ^0 polarization was ±0.10, which we have assigned as the associated systematic uncertainty $\delta\mathcal{P}'_{sys}$.

E. Final systematic uncertainty accounting

Our final systematic uncertainty accounting for the 5.754 GeV Λ and Σ^0 $\mathcal{P}'$ data is included in Table VI listing all of the sources discussed above. The final value for the total systematic uncertainty results from adding all the individual contributions in quadrature. (Additions in quadrature in Table VI are represented by the notation $\oplus$).

Category	Contribution	Systematic Uncertainty
Polarization Extraction	Functional Form	0.008
	Bin Size	0.018
	Asymmetry Parameter	0.02 $\mathcal{P}'_Y$
Beam-Related Factors	Beam Polarization	0.04 $\mathcal{P}'_Y$
Acceptance Function	Fiducial Cut Form	0.020
	Acceptance Correction	0.033
	Acceptance Cutoff	0.025
Background Contributions	Pion and Λ contamination	0.009 (Λ), 0.100 (Σ^0)
$\langle$ **Total Systematic Uncertainty** $\rangle$		0.051 (Λ), 0.112 (Σ^0) $\oplus$ 0.045$\mathcal{P}'_Y$

TABLE VI: Summary table of the systematic uncertainty assignments $\delta\mathcal{P}'_{sys}$ for the measured Λ and Σ^0 polarizations at 5.754 GeV. Note that the contributions from the uncertainties in the beam polarization and weak decay asymmetry parameter (given by $0.045\mathcal{P}'_Y$) are added in quadrature (represented by the $\oplus$ notation) to the other sources.

One way to verify the veracity of the final systematic uncertainty assignment is to look at the deviations of the normal components of the extracted Λ and Σ^0 polarizations (i.e. along the y' and y axes). Averaged over all analysis bins, the weighted mean of the $\mathcal{P}'_{y'}$ and $\mathcal{P}_y$ components for the Λ is 0.067 and for the Σ^0 is 0.134. Both of these values are consistent with our total systematic uncertainty assignments in Table VI. The extracted normal components for one of our data sorts for the Λ and Σ^0 hyperons are shown in Fig. 11.

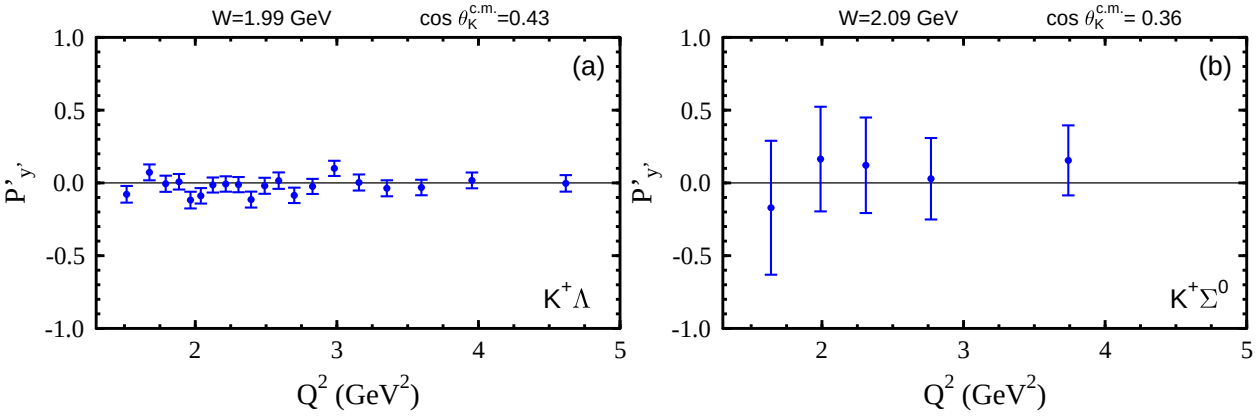

FIG. 11: (Color online) Distributions of the transferred Λ (a) and Σ^0 (b) polarization components $\mathcal{P}'_{y'}$ vs. Q^2 for two of our analysis bins. The error bars shown represent the statistical uncertainties only.

VII. RESULTS AND DISCUSSION

A. Λ polarization transfer

Our results for the transferred Λ polarization acquired at a beam energy of 5.754 GeV are shown in Figs. 12 through 15 compared to several model calculations. The error bars in these figures include statistical but not systematic uncertainties, which we estimate to be $0.051 \oplus 0.045\mathcal{P}'_\Lambda$ on the polarization. The full data set is contained in the CLAS database [50].

Figs. 12 and 13 show the dependence of $\mathcal{P}'_{x',z'}$ and $\mathcal{P}'_{x,z}$ with respect to $\cos\theta_K^{c.m.}$ for the three bin-averaged W and Q^2 values indicated in the figure. Fig. 12 shows that the value of $\mathcal{P}'_{z'}$ decreases smoothly with increasing scattering angle, whereas $\mathcal{P}'_{x'}$ decreases with increasing angle until $\cos\theta_K^{c.m.} \approx 0.8$, at which point it levels off to a value of about -0.5 over the range of $\cos\theta_K^{c.m.}$ covered by the experiment. The fact that the $\mathcal{P}'_{x'}$ data approach zero at $\cos\theta_K^{c.m.} = 1$ is simply a result of angular-momentum conservation, which also requires $\mathcal{P}'_{x'} = 0$ at $\cos\theta_K^{c.m.} = -1$. The dependence of the polarization along the (x, z) axes in Fig. 13 is qualitatively different. The polarization along $\mathcal{P}'_x$ is roughly zero everywhere, whereas $\mathcal{P}'_z$ is relatively constant (at least over the angle range $\cos\theta_K^{c.m.} > 0$ where the statistics are reasonable) with an average value of $\sim$0.6. This may be hinting at a simple reaction mechanism (see Section VII D).

The polarization with respect to W is shown in Fig. 14 for a beam energy of 5.754 GeV. Note that there is a strong dependence of the bin-averaged $\cos\theta_K^{c.m.}$ value with respect to W in these kinematics. The central $\cos\theta_K^{c.m.}$ values extracted from the analysis are reasonably represented by a fit to a second-order polynomial in W, with the fit shown in Fig. 14. In the plot of $\mathcal{P}'_{z'}$ (Fig. 14) we see that the polarization rises steadily from zero near threshold, followed by a dip at around $1.9 - 2.0$ GeV, and then remains constant at about 0.5 over the rest of the range. The $\mathcal{P}'_{x'}$ data are relatively constant at about -0.5 over most of the W range. We also note that the magnitude of $\mathcal{P}'_{z'}$ is nearly equal to $\mathcal{P}'_{x'}$, although with opposite sign, indicating equal strength in the $R_{TT'}^{z'0}$ and $R_{TT'}^{x'0}$ responses. With respect to the (x, z) axes (see Fig. 14), the polarization is roughly 0.6 and relatively constant along z and is consistent with zero along x. This latter point indicates either a perfect cancellation of the $R_{LT'}$ response functions (see Table III) or that they are each nearly zero.

The polarization as a function of Q^2 is shown in Fig. 15. The data are rather featureless and indicate almost no Q^2 dependence. Both $\mathcal{P}'_{z'}$ and $\mathcal{P}'_z$ are roughly 0.5, while $\mathcal{P}'_{x'} \approx -\mathcal{P}'_{z'}$, and $\mathcal{P}'_x$ is consistent with zero.

The $\mathcal{P}'_\Lambda$ data in Figs. 12 through 15 are compared against the theoretical models introduced in Section II. The MB hadrodynamic model [42] is indicated by the solid–black lines, the GLV Regge model [51] is indicated by the

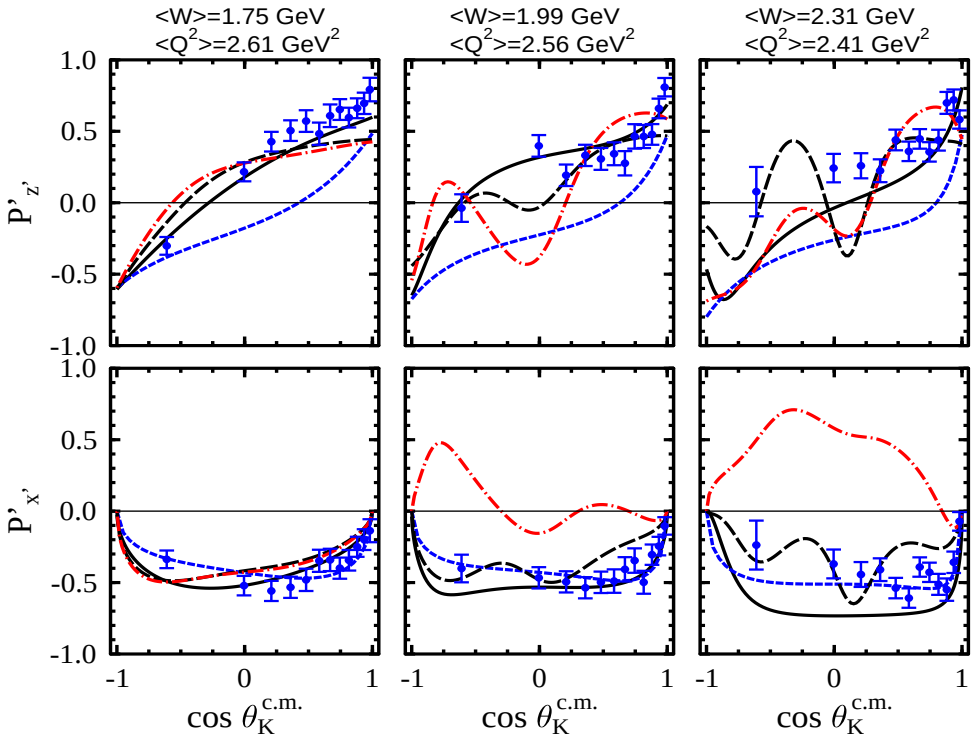

FIG. 12: (Color online) Transferred Λ polarization components $\mathcal{P}'$ with respect to the (x', z') axes vs. $\cos\theta_K^{c.m.}$ for three bin-averaged W/Q^2 values as indicated for a beam energy of 5.754 GeV. The curves are calculations from the MB isobar model [42] (solid – black), the GLV Regge model [51] (short dash – blue), and the RPR model [52] variant including a $P_{11}(1900)$ state (dot-dash – red) and a $D_{13}(1900)$ state (long dash – black).

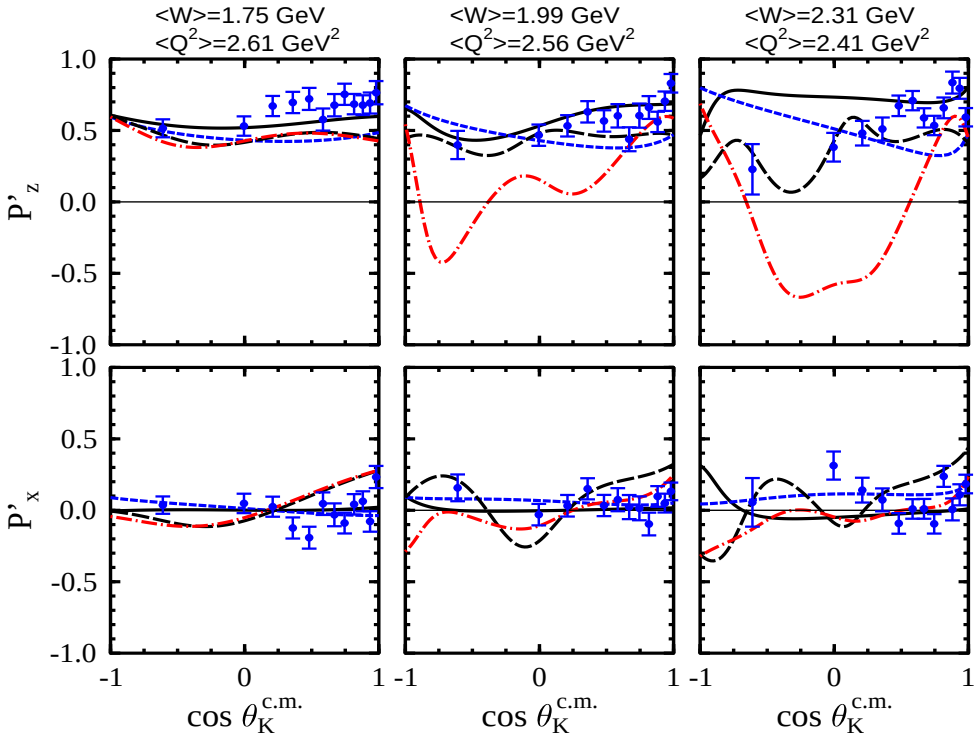

FIG. 13: (Color online) Transferred Λ polarization components $\mathcal{P}'$ with respect to the (x, z) axes vs. $\cos\theta_K^{c.m.}$ for three bin-averaged W/Q^2 values as indicated for a beam energy of 5.754 GeV. The model calculations are as indicated in Fig. 12.

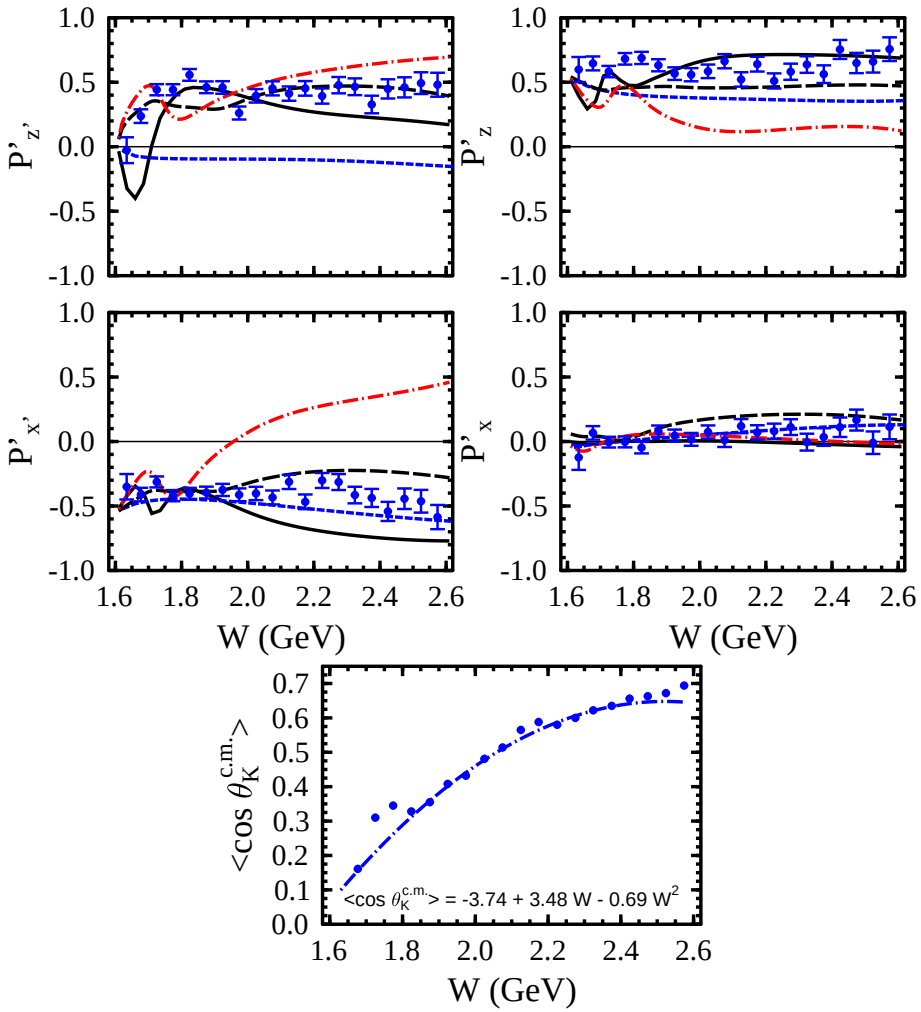

FIG. 14: (Color online) Transferred Λ polarization components $\mathcal{P}'$ with respect to the (x', z') axes (upper left panels) and (x, z) axes (upper right panels) vs. W (GeV) for $\langle Q^2 \rangle$=2.54 GeV^2 for a beam energy of 5.754 GeV. The bin-averaged $\cos\theta_K^{c.m.}$ values for each W point are shown in the lower plot. A fit to $\langle \cos\theta_K^{c.m.} \rangle$ is provided by a second-order polynomial in W as indicated on the plot. The model calculations are as indicated in Fig. 12.

short dash–blue lines, and the RPR model [52] is indicated by the dot-dash–red lines (P_{11} model variant) and by the long-dash–black lines (D_{13} model variant). The calculations qualitatively match the sign and trends of the data, but detailed comparisons indicate that these new polarization data can be used to further tune the models (e.g. the resonance parameters in the MB model and the RPR model) or indicate shortcomings in the dynamical description of the data (i.e. the pure t-channel description of the GLV Regge model).

Detailed comparisons of the individual models to these data are also useful to indicate specific shortcomings of the models. For example, comparisons of the MB model to the data show problems with the parameters for the resonances included below 2.0 GeV as indicated by both $\mathcal{P}'_{z'}$ and $\mathcal{P}'_{x'}$. The models also mostly fail to reproduce the data as a function of Q^2 (Fig. 15), which could indicate problems with the modeling of the non-resonant strength with increasing Q^2 or the description of the Q^2 evolution of the hadronic form factors.

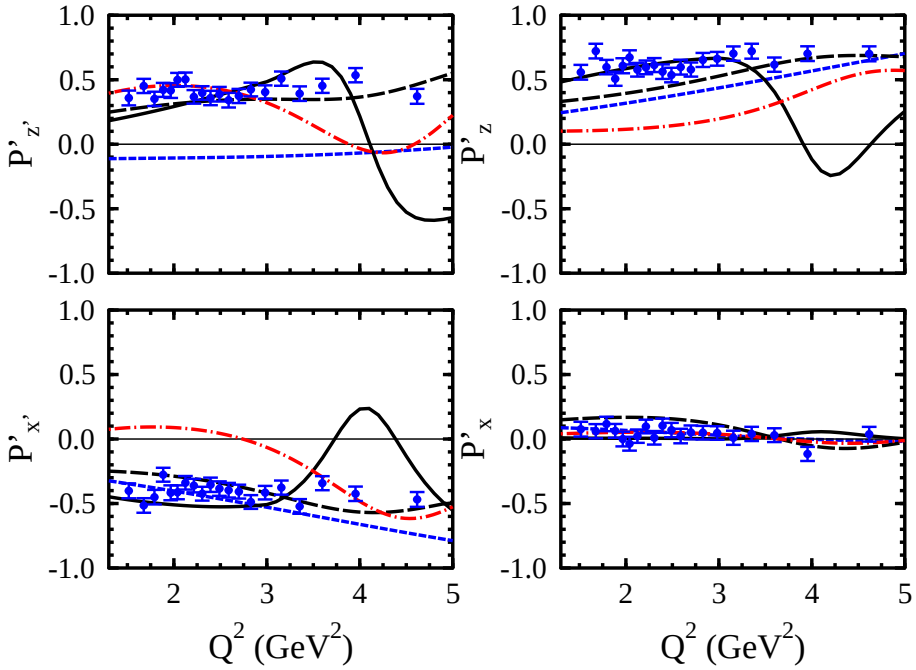

FIG. 15: (Color online) Transferred Λ polarization components $\mathcal{P}'$ with respect to the (x', z') axes (left panels) and (x, z) axes (right panels) vs. Q^2 (GeV^2) for $\langle W\rangle$=1.99 GeV and $\langle\cos\theta_K^{c.m.}\rangle$=0.43 for a beam energy of 5.754 GeV. The model calculations are as indicated in Fig. 12.

Comparisons of the GLV Regge model to the data indicate that a purely t-channel description of the $K^+\Lambda$ reaction is not adequate to reproduce the polarization results, even for this channel suspected to be predominantly governed by K and K^* exchange [6]. The s-channel resonance contributions still have important consequences for the interference observables. Whereas the GLV model produces a very smooth behavior for $\mathcal{P}'$ vs. W, $\cos\theta_K^{c.m.}$, and Q^2, the model typically underpredicts the strength and does not account for the detailed trends in the data. In some cases (e.g. Figs. 12, 14, and 15), the GLV model has the wrong sign compared to the data or has the wrong slope.

For the RPR calculation, two model variants are compared with the data. One employs a $P_{11}(1900)$ state. As was also seen in comparison with the CLAS $\sigma_{LT'}$ data [34], the model variant with the P_{11} (dot-dash – red) is strongly ruled out by the polarization data. The second model variant (long dash – black) employs the $D_{13}(1900)$ state proposed by Mart and Bennhold (see Section II). This model provides a reasonable description of the polarization data over the full kinematic phase space. The only issue with this model, which cannot be fully clarified by these data, is the strong interference effects seen in the calculations at higher W (see Figs. 12 and 13).

B. Σ^0 polarization transfer

Our results for the transferred Σ^0 polarization acquired at a beam energy of 5.754 GeV are shown in Figs. 16 through 18 compared to several model calculations. The error bars in these figures include statistical but not systematic

uncertainties, which we estimate to be $0.112 \oplus 0.045\mathcal{P}'_{\Sigma}$ on the polarization (see Section VI). The full data set is contained in the CLAS database [50].

Fig. 16 shows the dependence of $\mathcal{P}'_{x',z'}$ and $\mathcal{P}'_{x,z}$ with respect to $\cos\theta_K^{c.m.}$ and Fig. 17 shows the polarization with respect to W. As with the Λ results, $\cos\theta_K^{c.m.}$ values at each W point are well represented by a low-order polynomial in W (given in Fig. 17). Fig. 18 shows the polarization with respect to Q^2.

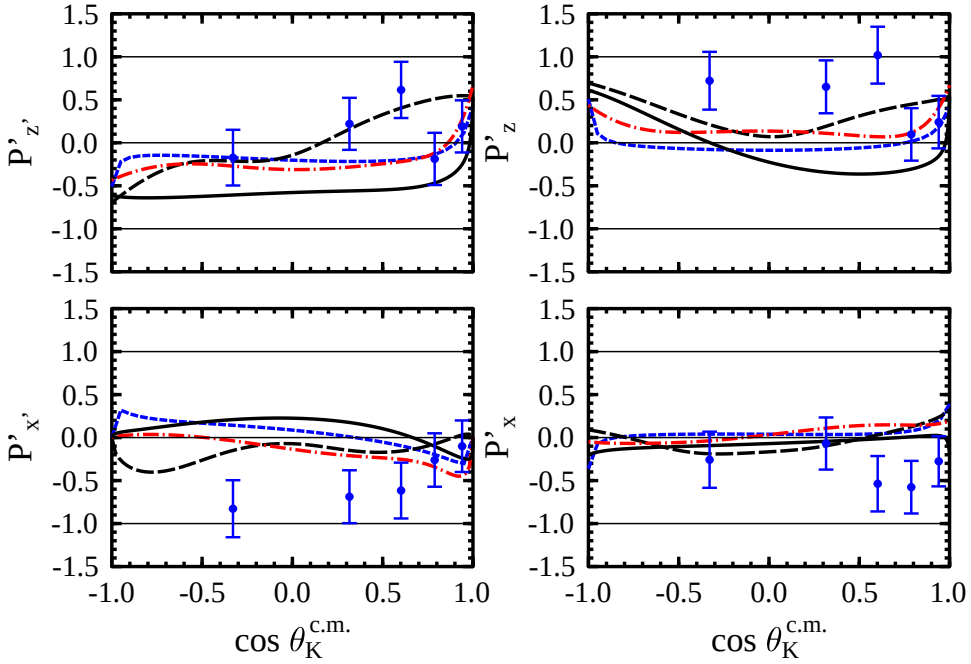

FIG. 16: (Color online) Transferred Σ^0 polarization components $\mathcal{P}'$ with respect to the (x', z') (left) and (x, z) (right) axes vs. $\cos\theta_K^{c.m.}$ at $\langle Q^2\rangle$=2.5 GeV^2 and $\langle W\rangle$=2.1 GeV for a beam energy of 5.754 GeV. The curves are calculations from the MB isobar model [42] (solid – black), the GLV Regge model [51] (short dash – blue), and the RPR model [52] with a missing $P_{11}(1900)$ state (dot-dash – red) and a missing $D_{13}(1900)$ state (long dash – black).

An important point to note is the rather sizable statistical uncertainties on the Σ^0 data. This arises not due to the limitations of the Σ^0 data sample (which has roughly 3000 counts in each analysis bin), but rather due to the scaling by $\alpha_\Lambda/\alpha_\Sigma$ in Eq.(26). It should also be made clear that the `e1-6` running period at CLAS represented a very lengthy run period (extending over 4 months) that recorded nearly 5 billion triggers. Given the effect of the Λ background beneath the Σ^0 peak, CLAS will likely not be able to provide more precise electroproduction data for this observable.

Figs. 16 through 18 indicate that the measured Σ^0 transferred polarization tends to have the same sign as the Λ polarization for the different axes. More quantitative statements cannot be made given the statistical quality of the data. In comparing the data to the models, with the possible exception of the MB model (solid black), one sees that they qualitatively match the sign and trends of the data, as was the case for the Λ data. However, as the $\mathcal{P}'_{\Sigma}$ observable has not been measured before, the results can still serve to provide at least loose constraints on the theoretical models. Certainly the $\mathcal{P}'_{\Lambda}$ data can be used to improve the knowledge of the contributing N^* states by allowing for improved

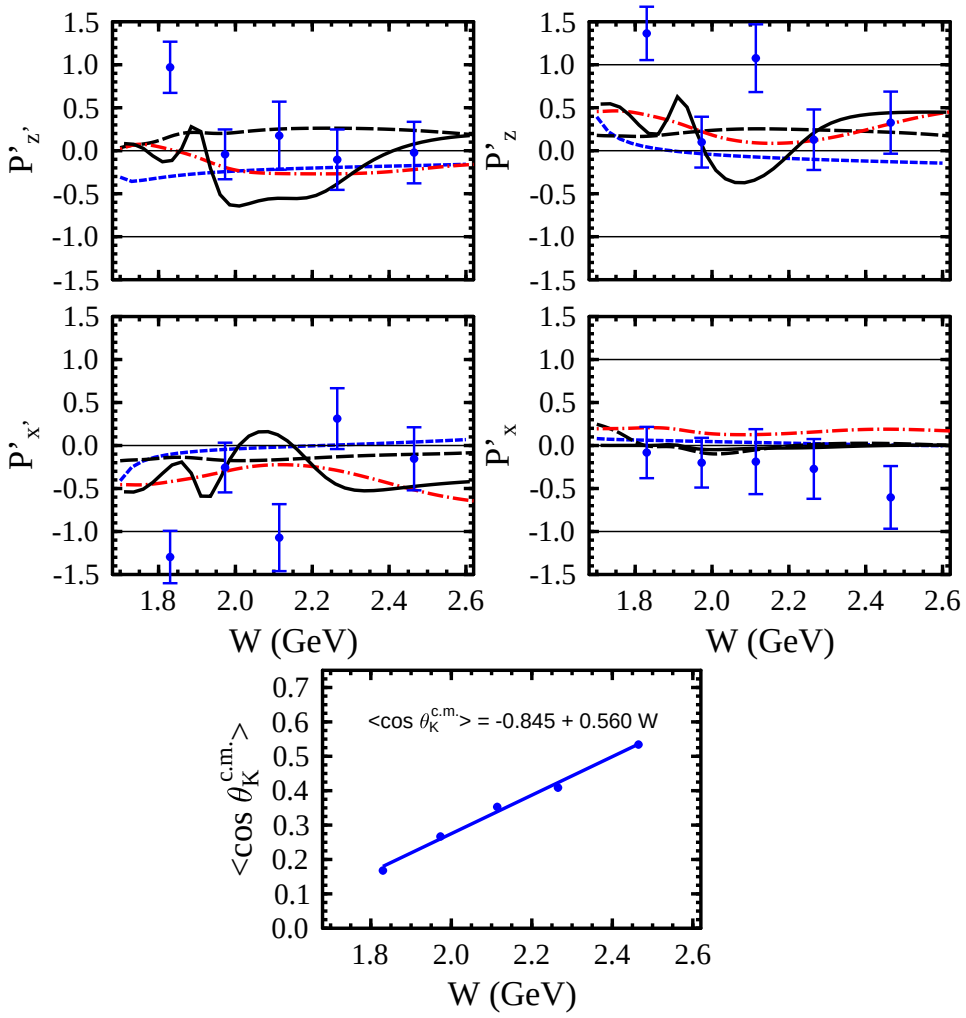

FIG. 17: (Color online) Transferred Σ^0 polarization components $\mathcal{P}'$ with respect to the (x', z') (left) and (x, z) (right) axes vs. W (GeV) at $\langle Q^2 \rangle$=2.5 GeV^2 for a beam energy of 5.754 GeV. The bin-averaged $\cos\theta_K^{c.m.}$ value for each W point is represented by a second-order polynomial in W. The model calculations are as indicated in Fig. 16.

descriptions of the associated form factors and the $g_{KN\Lambda}$ coupling strengths. These improvements can then be used in the Σ^0 modeling, which typically employ the same set of N^* states for both the $K^+\Lambda$ and $K^+\Sigma^0$ final states.

C. Extraction of the ratio of σ_L/σ_T

In order to extract $R_\sigma = \sigma_L/\sigma_T$ at $\cos\theta_K^{c.m.} = 1$, we must first extrapolate $\mathcal{P}'_{z'}$ (or $\mathcal{P}'_z$) to $\cos\theta_K^{c.m.} = 1$. However, because of statistical fluctuations in the data and finite angle resolution effects, extrapolations for $\mathcal{P}'_{z'}$ give slightly different results than extrapolations for $\mathcal{P}'_z$. Following the procedure defined in Ref. [23], the extrapolation is actually performed by summing the $\mathcal{P}'_{z'}$ and $\mathcal{P}'_z$ components into a new quantity R_{sum} (see Table III for component definitions)

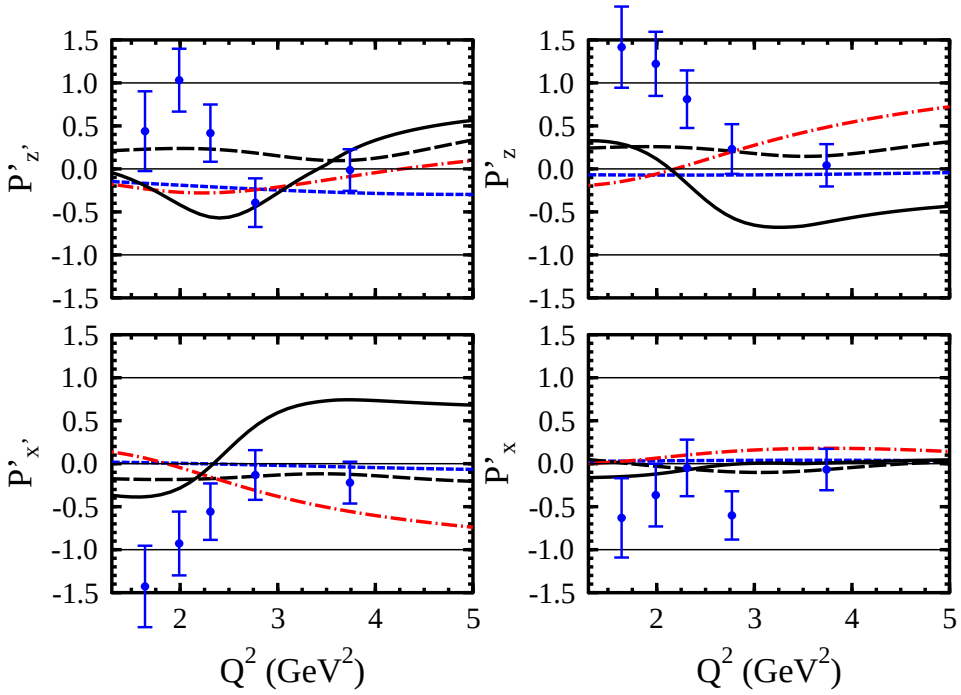

FIG. 18: (Color online) Transferred Σ^0 polarization components $\mathcal{P}'$ with respect to the (x', z') (left) and (x, z) (right) axes vs. Q^2 (GeV^2) at $\langle W\rangle$=2.09 GeV and $\langle \cos\theta_K^{c.m.}\rangle = 0.36$ at a beam energy at 5.754 GeV. The model calculations are as indicated in Fig. 16.

given by

$$R_{sum} \equiv \frac{(\mathcal{P}'_{z'} + \mathcal{P}'_z)\sigma_U}{c_0} = \mathcal{K}[(1+\cos\theta_K^{c.m.})R_{TT'}^{z'0} - R_{TT'}^{x'0}\sin\theta_K^{c.m.}]. \tag{34}$$

From the extrapolated value of R_{sum} at $\cos\theta_K^{c.m.} = 1$, Eq.(34) can then be inverted to determine $\mathcal{P}'_{z'}$ (or equivalently $\mathcal{P}'_z$), which in turn is used to extract R_σ using Eq.(9).

An additional benefit of using this form is that Eqs.(7) and (9) provide important and useful constraints on R_{sum} at $x \equiv \cos\theta_K^{c.m.} = \pm 1$. At $x = -1$, the sum of the polarizations must be zero, according to Eq.(7), leading to $R_{sum}(x = -1) = 0$. Since both σ_L and σ_T must be positive definite, then R_σ (see Eq.(9)) must also be positive definite, which leads to $R_{sum} \leq 2\sigma_U$ for $x = 1$. Note also that as both σ_L and σ_T must be positive definite, Eq.(9) constrains both the Λ and Σ^0 hyperon polarization components $\mathcal{P}'_z$ to be between 0 and c_0. This argument confirms the sign of the hyperon polarization is correct in our analysis.

Besides the explicit $\theta_K^{c.m.}$ dependence shown in Eq.(34) and in the response functions, the CGLN amplitudes contain additional $\theta_K^{c.m.}$ dependence (as well as Q^2 and W dependence) [35]. This suggests that Eq.(34) can then be fit with polynomials in $x = \cos\theta_K^{c.m.}$, provided we have prior knowledge of the σ_U term. In the case of the 4.261 GeV data, we can use the previously published CLAS results [6], while for the 5.754 GeV data, we have to use models to provide

σ_U at our kinematic points.

The number of terms to include in a polynomial fit to Eq.(34) is ultimately governed by the reaction dynamics. The explicit $\theta_K^{c.m.}$ dependence alone suggests at least a third-order polynomial. However, given the limited number of polarization data points, the number of terms in any fit leading to a meaningful extrapolation to $\cos\theta_K^{c.m.} = 1$ must also be limited. We begin by considering third-order fits of the form

$$R_{sum} = a_0 + a_1 x + a_2 x^2 + a_3 x^3, \tag{35}$$

where $a_{i=0\rightarrow 3}$ represent the fit coefficients. However, applying the constraint $R_{sum} = 0$ at $x = -1$ implies $a_1 = a_0 + a_2 - a_3$.

We have done a series of fits to the data points representing R_{sum} in which we varied the number of terms in the fits, while imposing a penalty on the χ^2 if a fit returned an unphysical value at $x = 1$. The penalty was chosen to be large enough to force non-negative values of R_σ. It should be noted that only one of the fits (5.754 GeV data at W=1.75 GeV and Q^2=2.61 GeV^2) required the imposition of a penalty. In determining the optimal number of parameters in the fit for each W, we simply used the number of parameters that produced the smallest minimized χ^2_ν (χ^2 per degree of freedom). All three of the 4.261 GeV fits favored a second-order fit ($a_3 = 0$), while all three of the 5.754 GeV fits favored a third-order fit.

The $\mathcal{P}'_{z'}$ and $\mathcal{P}'_z$ data from the 4.261 GeV data set are shown in Fig. 19 with respect to $\cos\theta_K^{c.m.}$. The full set of 4.261 GeV polarization transfer data for the (x', z') and (x, z) axes with respect to W and $\cos\theta_K^{c.m.}$ is provided in Ref. [50]. The $\mathcal{P}'_{z'}$ and $\mathcal{P}'_z$ data from the 5.754 GeV data set are shown in Figs. 12 and 13. We should point out that the $\mathcal{P}'_{z'}$ and $\mathcal{P}'_z$ results come from the same data. Therefore, these observables are not independent. They do, however, measure different quantities (as seen in Table III) since they are projections onto different axes. In adding these together to form R_{sum}, the uncertainties from $\mathcal{P}'_{z'}$ and $\mathcal{P}'_z$ were added together.

The results of our fits to the 4.261 GeV and 5.754 GeV data are shown in Fig. 20 (heavy solid lines) along with an error band (light solid lines). The error bands include uncertainties both from the fitting of Eq.(35), and, for the 4.261 GeV data, contributions from uncertainties in the fits of the cross section data. The latter contribution to the uncertainties is about half that of the former. The error band indicates that the extrapolation to $x = 1$ is well constrained. For the 5.754 GeV data we display the fit using the calculated cross section for one particular choice of the MB model [26], which allows for different choices of form factors and couplings.

Table VII shows the resulting χ^2_ν, the polarization extrapolated to $x = 1$, and R_σ. Since the 5.754 GeV data

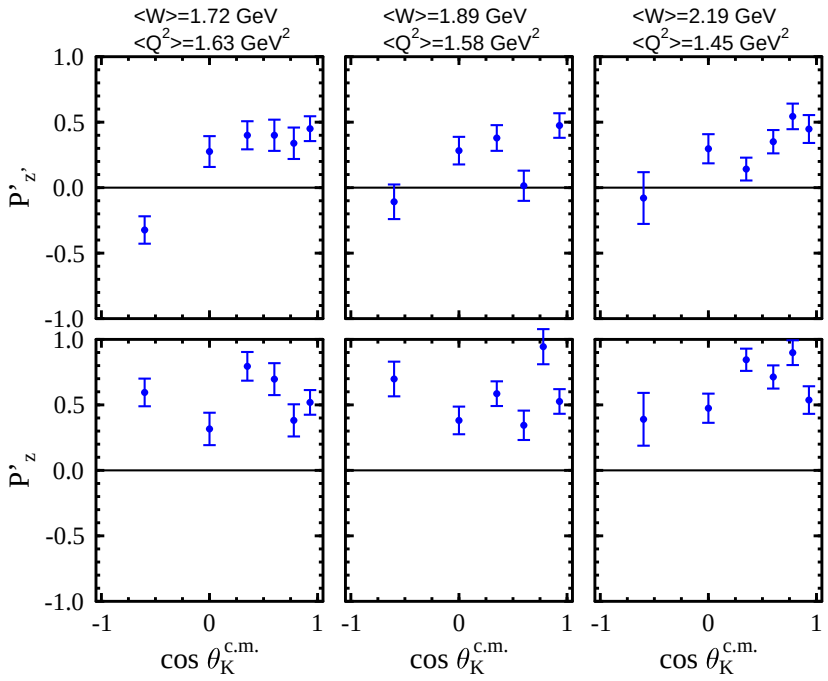

FIG. 19: (Color online) Transferred Λ polarization components $\mathcal{P}'$ with respect to the (z', z) axes vs. $\cos\theta_K^{c.m.}$ for three bin-averaged W/Q^2 values as indicated for a beam energy of 4.261 GeV.

E_b (GeV)	$\langle W\rangle$ GeV	$\langle Q^2\rangle$ GeV^2	χ^2_ν	$\mathcal{P}'_{z',z}(x=1)$	R_σ
4.261	1.72	1.63	0.77	0.451±0.066	0.533±0.270±0.326
	1.89	1.58	5.69	0.440±0.063	0.870±0.329±0.401
	2.18	1.45	0.87	0.486±0.062	1.348±0.404±0.515
5.754	1.75	2.61	1.11	0.607±0.070	0.000±0.092±0.156
	1.98	2.56	2.76	0.610±0.065	0.176±0.088±0.209
	2.31	2.31	2.79	0.470±0.053	0.637±0.120±0.445

TABLE VII: Transferred polarization at $x = \cos\theta_K^{c.m.} = 1.0$ extrapolated from the fits described in the text along with the resulting value of the ratio of longitudinal to transverse structure functions. Uncertainties on $\mathcal{P}'_{z',z}$ are the combined uncertainties arising from the fit to the polarization data and the uncertainties in the cross section data. The first uncertainty on R_σ is the statistical uncertainty (from the fit), while the second represents an estimated systematic uncertainty.

required a model for σ_U, we repeated the fit for five different parameter set choices within the framework of the MB model [26]. Thus, the 5.754 GeV results in the table reflect the average values of χ^2_ν, the polarization extrapolated to $x = 1$, and R_σ for different models. We estimated the model uncertainty by using the standard deviation of R_σ from using the five different models.

Inserting the extrapolated polarizations into Eq.(9), we can determine the ratio R_σ. These values are shown in the last column of Table VII, along with the combined uncertainties of the polarization and cross section fits, and an estimated systematic uncertainty. The systematic uncertainty includes a contribution assuming a 10% relative systematic uncertainty in the polarization data.

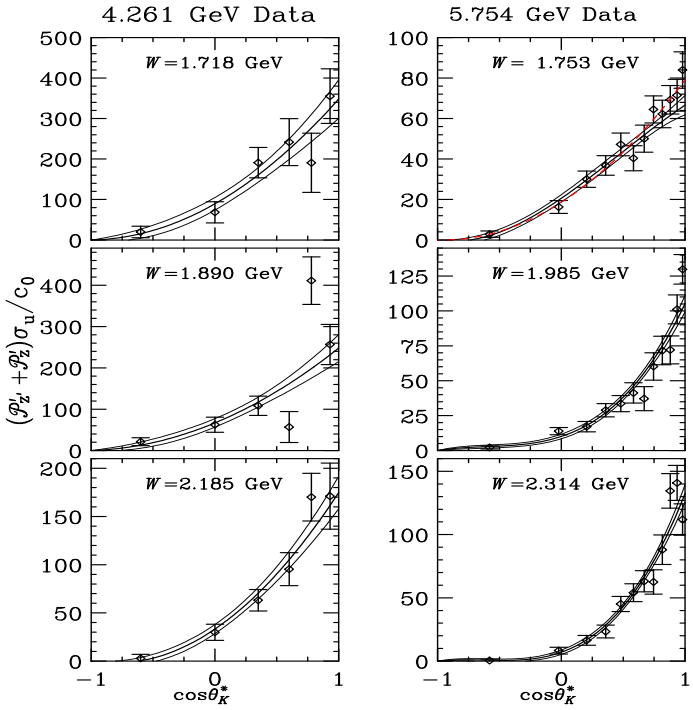

FIG. 20: (Color online) R_{sum} (defined in Eq.(34)) vs. $\cos\theta_K^{c.m.}$ for the 4.261 GeV and 5.754 GeV data along with our fits (heavy solid lines) and the error band resulting from the fit uncertainties (light solid lines). The dashed red line in the upper right panel indicates the result of removing the $x = 1$ constraint in the fit.

The resulting values for R_σ are plotted in Fig. 21. For comparison, we have also included the previously published data [6, 24, 37]. However, only the filled points are at or near the common value of W ≈1.84 GeV. Other than these filled points, one should not take any trends in the data too seriously since the data from this analysis cover a large range in W (1.72 to 2.31 GeV).

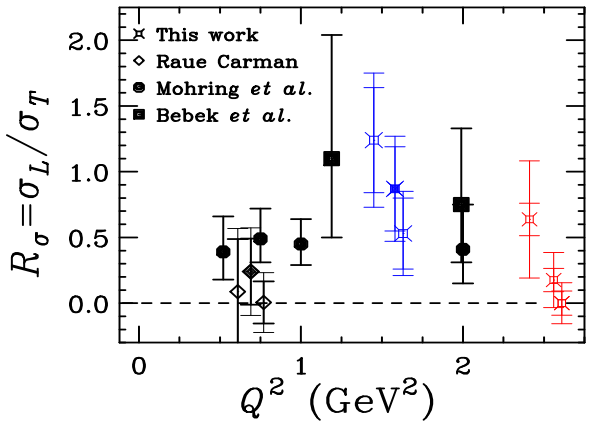

FIG. 21: (Color online) Ratio of longitudinal to transverse structure functions at $\theta_K^{c.m.} = 0°$ vs. Q^2. The blue cross data points (about Q^2=1.5 GeV^2) are for 4.261 GeV and the red cross points (about Q^2=2.5 GeV^2) are for 5.754 GeV. The inner error bars on our points represent the statistical uncertainties arising from the fit and the outer error bars represent the combination of statistical and estimated systematic uncertainties. The triangles are data from CLAS [6], the solid circles are data from Mohring *et al.* [24], the solid squares are data from Bebek *et al.* [37], and the diamonds are data from Raue and Carman [23]. All of the filled points are near a common value of W ≈1.84 GeV.

Our new results from the data sets at 4.261 and 5.754 GeV are in reasonable accord with the existing measurements

of σ_L/σ_T from Bebek *et al.* [37] and Mohring *et al.* [24]. Looking at the results for $W \approx$1.84 GeV, the ratio rises with Q^2 up to $Q^2 \sim 1.5$ GeV^2 and thereafter seems to fall off, suggesting an interesting and non-trivial dependence on Q^2, but the measurement accuracy is not adequate to quantify this observation. Alternatively, we point out that our data also seem to suggest a rapid rise of σ_L/σ_T with W as was suggested in our previous publication [6], however again, we lack the statistical and systematic precison to make a more definitive conclusion. Note that the σ_L/σ_T data from Ref. [6] at Q^2=1.0 GeV^2 cannot be directly compared to these data as the most forward angle point in that work is $\cos\theta_K^{c.m.}$=0.90.

The data of Fig. 21 imply that for at least a limited Q^2 interval, the longitudinal structure function becomes sizable. This structure function is expected to be very sensitive to the kaon form factor [53]. A recently conducted experiment in Hall A at Jefferson Laboratory [54] has as one of its main goals a Rosenbluth separation at several values of momentum transfer t leading to a Chew-Low extrapolation [55] of the kaon form factor. However, this method relies on having small *relative* uncertainties for σ_L, which will not be the case when σ_L is itself small. These new results indicate that the successful extraction of the form factor may only be possible in a limited kinematic range.

D. Partonic models of the process

All of the models introduced thus far in this work have been used to indicate the strong sensitivity of these polarization data to the underlying s-channel resonant terms that contribute in the intermediate state of the $\gamma^* p \to K^+ Y$ process. The precision and broad kinematic coverage of the data from Ref. [6] have indicated that the $K^+\Lambda$ final state is dominated by t-channel kaon exchange. However, there are important contributions from s-channel processes that must be taken into account to describe both the cross section and polarization data in detail.

In contradistinction to the hadronic models, and as noted earlier and introduced in Ref. [10], our data indicate the Λ polarization is maximal along the virtual photon direction (see results for $\mathcal{P}'_z$ in Figs. 13, 14, and 15), suggesting a simple phenomenology. In fact, the Λ polarization is essentially unity if the virtual photon depolarization factor is taken into account (see Section IV D). The lack of a strong W and Q^2 dependence is an indication that the data might be more economically described in a flux-tube strong-decay framework. There is growing evidence that the relevant degrees of freedom to describe the phenomenology of hadronic decays are constituent quarks bound by a gluonic flux-tube [56]. Properties of the flux-tube can be determined by studying $q\bar{q}$ pair production, since this is widely believed to produce the color field neutralization that breaks the flux-tube. Since the 1970's, it has been argued that a quark pair with vacuum quantum numbers is responsible for breaking the color flux-tube (the $^3P_0$ model [57]).

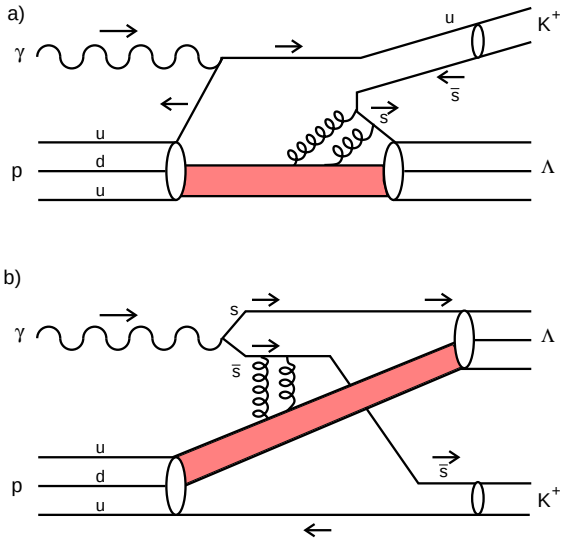

FIG. 22: (a) A model of the reaction where a circularly polarized virtual photon strikes an oppositely polarized u quark inside the proton. The spin of this quark flips and the quark recoils from its neighbors. An $s\bar{s}$ quark pair is created from a $J^\pi = 0^-$ two-gluon exchange (in lowest order) to produce the final-state K^+ and Λ hyperon. (b) A model of the reaction where an $s\bar{s}$ quark pair is produced from a circularly polarized real photon that hadronizes such that the s quark in the Λ retains its full polarization after being "precessed" by a spin-orbit interaction, while the $\bar{s}$ quark ends up in the spinless kaon. In both pictures the shaded band represents a spinless $u - d$ diquark system.

This simple phenomenology of the Λ polarization data has led two groups within the CLAS Collaboration to develop semi-classical models based on partonic degrees of freedom to describe the associated reaction mechanism. In the model of Carman *et al.* [10, 58] (shown in Fig. 22(a)), it is assumed that the cross section is dominated by photoabsorption by a u quark. Due to the helicity-conserving vector interaction, the u quark becomes polarized along the photon direction ($+z$). Hadronization into the $K^+\Lambda$ final state proceeds with the production of an $s\bar{s}$ pair that breaks the color flux-tube. Because the u quark hadronizes as a pseudoscalar K^+, the $\bar{s}$ quark spin is required to be opposite to that of the u quark, i.e. in the $-z$ direction. In the non-relativistic quark model, the entire spin of the Λ is carried by the s quark. Since the Λ polarization is in the $+z$ direction, seen by the fact that $\mathcal{P}'_z > 0$, it was concluded that the s and $\bar{s}$ spins were anti-aligned when they were created, if the hadronization process did not flip or rotate their spins. Note that Liang and Boros also posit a two-step process for the production of transversely polarized Λ hyperons in the exclusive $pp \to pK^+\Lambda$ reaction [59], and come to a similar conclusion that the $s\bar{s}$ quark pair must have been produced with spins anti-aligned. More recently, Λ polarization has been interpreted within an instanton interaction model [60], which also is assumed to occur with the production of an anti-aligned $s\bar{s}$ quark pair. A dominance of spin anti-alignment for the s and $\bar{s}$ quarks would not be consistent with the $S = 1$ $^3P_0$ operator [25], which predicts a 2:1 mixture of $s\bar{s}$ quarks produced with spins aligned vs. anti-aligned if the orbital substates are equally populated. Along with other observations of failure of the $^3P_0$ model (e.g. explaining $\pi_2 \to \rho\omega$ decay [25]),

the applicability of the $^3P_0$ model in describing all hadronic decays is brought into doubt if this model is appropriate.

Extensive photoproduction data for the transferred polarization for the $K^+\Lambda$ final state has also been published from CLAS [9]. These data also indicate that the Λ polarization is predominantly in the direction of the spin of the incoming photon, independent of the center-of-mass energy or meson production angle. Based on these data, Schumacher has introduced a different model [58, 61] to explain the Λ polarization results. In this model, shown in Fig. 22(b), the produced $s\bar{s}$ pair is created in a $^3S_1$ configuration (J=1, S=1, L=0, i.e. $J^\pi = 1^-$). Here, following the principle of vector meson dominance, the real photon fluctuates into a virtual ϕ meson that carries the polarization of the incident photon. Therefore, the quark spins are in the direction of the spin of the photon before the hadronization interaction. The s quark of the pair merges with the unpolarized diquark within the target proton to form the Λ baryon, and the $\bar{s}$ quark merges with the remnant u quark of the proton to form a spinless K^+ meson.

The two model interpretations, while able to predict the correct sign for the Λ polarization transfer, nevertheless describe very different physical processes. Both assume that the mechanism of spin transfer to the Λ hyperon involves a spectator $J^\pi = 0^+$ diquark system. The main difference is the role of the third quark. Neither model specifies a detailed dynamical mechanism. If we take the gluonic degrees of freedom into consideration, the model of Carman *et al.* [10] can be realized in terms of a possible mechanism in which a colorless $J^\pi = 0^-$ two-gluon subsystem is emitted from the spectator diquark system and produces the $s\bar{s}$ pair as illustrated in Fig. 22(a). To the same order of gluon coupling, the model of Schumacher [61] is the quark-exchange mechanism illustrated in Fig. 22(b), again mediated by a two-gluon exchange. The amplitudes corresponding to these diagrams may both be present in the production, in principle, and could contribute at different levels depending on the reaction kinematics.

Extending these studies to the $K^{*+}\Lambda$ exclusive final state should be revealing. In the Carman *et al.* model, the spin of the u quark is unchanged when changing from a scalar K^+ to a vector K^{*+}. If the $s\bar{s}$ quark pair is produced with spins anti-aligned, then the spin direction of the Λ should flip. On the other hand, in the Schumacher model, the u quark in the kaon is only a spectator; changing its spin direction – and thus changing the K^+ to a K^{*+} – should not change the Λ spin direction. Thus there are ways to disentangle the relative contributions and to better understand the reaction mechanism and dynamics underlying the associated strangeness production reaction. Analyses at CLAS are underway to extract the polarization transfer to the hyperon in the $K^{*+}\Lambda$ final state.

In developing the quark model interpretations of polarization transfer, we also need to consider the phenomenology of the $K^+\Sigma^0$ results. As shown in this work, and much more clearly in the CLAS photoproduction data [9], the $K^+\Sigma^0$ polarization transfer is very similar in magnitude *and* sign to the $K^+\Lambda$ data. We might expect that when the Λ and

Σ^0 polarization transfers in these reactions point in opposite directions and have the same magnitudes, this would then give more weight to the modeling of the polarizations originating from a quark level interaction, in particular associated with the strange quark spin. However, even though this is not what is observed in the data, we should realize that the spin state of the Σ^0 hyperon is not determined by the strange quark alone, but a combination of the s quark spin and the triplet ud quark spin. Thus the models of Fig. 22 are not directly applicable for $K^+\Sigma^0$ production.

Understanding a process of this sort through partonic models can shed light on quark-gluon dynamics in a domain usually thought to be dominated by traditional meson and baryon degrees of freedom. These issues are relevant to better understand strong interactions and hadroproduction in general due to the non-perturbative nature of QCD for CLAS kinematics. We eagerly await further experimental studies and new theoretical efforts to understand which multi-gluonic degrees of freedom dominate in quark-pair creation and their role in strangeness production, as well as the appropriate mechanism (or mechanisms) for the dynamics of spin transfer in hyperon production.

VIII. SUMMARY AND CONCLUSIONS

In this paper we have provided extensive new data at 4.261 and 5.754 GeV for the beam-recoil hyperon polarization transfer for the reaction $p(\vec{e}, e'K^+)\vec{\Lambda}$ studying its dependence on the kinematic variables Q^2, W, and $\cos\theta_K^{c.m.}$. These data add to the earlier 2.567 GeV CLAS data results from Ref. [10]. In addition, we have provided the first-ever polarization transfer data for the reaction $p(\vec{e}, e'K^+)\vec{\Sigma}^0$. These new data sets span a range of momentum transfer Q^2 from 0.7 to 5.4 GeV^2, invariant energy W from 1.6 to 2.6 GeV, and the full K^+ center-of-mass angular range.

Our data have been compared to predictions from several available theoretical models that have varying sensitivities to the s-channel resonance contributions. The increased statistical precision of these new data will enable improved fits either for effective Lagrangian models or for coupled-channels model fits incorporating both photo- and electroproduction data that will be carried out by several groups in the near future [62], including the Excited Baryon Analysis Center (EBAC) [63] at Jefferson Laboratory. The analysis of the full set of the world's data in this manner is essential to map out the full spectrum of excited states of the nucleon to better determine the structure of the nucleon and its associated degrees of freedom, both of which are necessary to better understand the strong interaction and QCD.

The new CLAS Λ polarization data sets at 4.261 and 5.754 GeV have also been used to extract the longitudinal-to-transverse structure function ratio at $\theta_K^{c.m.} = 0^\circ$ in the Q^2 range from 1.5 to 2.5 GeV^2, extending the existing CLAS measurements taken at 2.567 GeV near Q^2=1.0 GeV^2. These new data, given the statistical uncertainties, could indicate a non-trivial Q^2 evolution of the structure function ratio in the range from Q^2=0.7 to 2.5 GeV^2, that

peaks near unity at Q^2=1.5 GeV^2. These results indicate that extraction of the kaon form factor using the standard Chew-Low extrapolation technique can only be carried out in the limited kinematic range where σ_L is sizable.

Finally, the data have been compared to two simple semi-classical partonic models including multi-gluon exchange that were designed to account for the strikingly simple phenomenology seen in the kinematic dependence of the polarization data. While the two models make very different assumptions regarding the reaction mechanism leading to production of the $K^+\Lambda$ final state and different quantum numbers of the produced $s\bar{s}$ pair, we have provided suggestions for testing them by comparing polarization data for $K^+\Lambda$ to $K^{*+}\Lambda$ final states. Disentangling the true reaction dynamics in a partonic model is relevant to probe the appropriate quark-pair creation operator that governs the transitions to the final state particles and to shed light on the relevance of quark-gluon dynamics in a domain thought to be dominated by meson/baryon degrees of freedom.

We would like to acknowledge the outstanding efforts of the staff of the Accelerator and the Physics Divisions at Jefferson Lab that made this experiment possible. This work was supported in part by the U.S. Department of Energy, the National Science Foundation, the Italian Istituto Nazionale di Fisica Nucleare, the French Centre National de la Recherche Scientifique, the French Commissariat à l'Energie Atomique, and the Korean Science and Engineering Foundation. The Southeastern Universities Research Association (SURA) operated the Thomas Jefferson National Accelerator Facility for the United States Department of Energy under contract DE-AC05-84ER40150.

---

[1] S. Capstick and W. Roberts, Phys. Rev. D **58**, 074011 (1998).

[2] N. Isgur, Proceedings of the NSTAR 2000 Conference, eds. V.D. Burkert, L. Elouadrhiri, J.J. Kelly, and R. Minehart, (World Scientific, Singapore, 2001), p. 403.

[3] R. Koniuk and N. Isgur, Phys. Rev. D **21**, 1868 (1980).

[4] S. Capstick and W. Roberts, Phys. Rev. D **49**, 4570 (1994).

[5] C. Amsler *et al.*, Particle Data Group, Phys. Lett. B **667**, 1 (2008).

[6] P. Ambroziewicz *et al. (CLAS Collaboration)*, Phys. Rev. C **75**, 045203 (2007).

[7] T. Corthals *et al.*, Phys. Lett. B **656**, 186 (2007).

[8] J.W.C. McNabb *et al. (CLAS Collaboration)*, Phys. Rev. C **69**, 042201(R) (2004).

[9] R.K. Bradford *et al. (CLAS Collaboration)*, Phys. Rev. C **75**, 035205 (2007).

[10] D.S. Carman *et al. (CLAS Collaboration)*, Phys. Rev. Lett. **90**, 131804 (2003).

[11] V.A. Nikonov *et al.*, Phys. Lett. B **662**, 245 (2008).

[12] A.V. Anisovich *et al.*, Eur. Phys. J. A **24**, 111 (2005).

[13] A.V. Anisovich *et al.*, Eur. Phys. J. A **25**, 427 (2005).

[14] G. Penner and U. Mosel, Phys. Rev. C **66**, 055212 (2002).

[15] W. Chiang *et al.*, Phys. Rev. C **69**, 065208 (2004).

[16] V. Shklyar, H. Lenske, and U. Mosel, Phys. Rev. C **72**, 015210 (2005).

[17] B. Julia-Diaz *et al.*, Nucl. Phys. A **755**, 463 (2005); B. Julia-Diaz *et al.*, Phys. Rev. C **73**, 055204 (2006).

[18] A.V. Sarantsev *et al.*, Eur. Phys. J. A **25**, 441 (2005).

[19] A.V. Anisovich *et al.*, Eur. Phys. J. A **34**, 243 (2007).

[20] P. Nadel-Turonski, B.L. Berman, D. Ireland, Y. Ilieva, and A. Tkabladze, JLab experiment E06-103, "Kaon Production on the Deuteron Using Polarized Photons".

[21] F.J. Klein and L. Toder, JLab experiment E02-112, "Search for Missing Nucleon Resonances in Hyperon Photoproduction".

[22] F.J. Klein, and A.M. Sandorfi, JLab experiment E06-101, "N^* Resonances in Pseudoscalar Meson Photoproduction from Polarized Neutrons in $\vec{H} \cdot \vec{D}$ and a Complete Determination of the $\gamma n \to K^0\Lambda$ Amplitude".

[23] B.A. Raue and D.S. Carman, Phys. Rev. C **71**, 065209 (2005).

[24] R.M. Mohring *et al.*, Phys. Rev. C **67**, 055205 (2003).

[25] T. Barnes, AIP Conf. Proc. **619**, 447 (2002).

[26] H. Haberzettl *et al.*, Phys. Rev. C **58**, R40 (1998); T. Mart and C. Bennhold, Phys. Rev. C **61**, 012201 (2000).

[27] R.K. Bradford *et al. (CLAS Collaboration)*, Phys. Rev. C **73**, 035202 (2006).

[28] M.Q. Tran *et al.*, Phys. Lett. B **445**, 20 (1998).

[29] B. Saghai, AIP Conference Proceedings **594**, 421 (2001).

[30] V. Shklyar and U. Mosel, Eur. Phys. J. A **21**, 445 (2004).

[31] T. Mart and A. Sulaksono, Phys. Rev. C **74**, 055203 (2006).

[32] D.G. Ireland, S. Janssen, and J. Ryckebusch, Nucl. Phys. A **740**, 147 (2004).

[33] M. Guidal, J.M. Laget, and M. Vanderhaegen, Nucl. Phys. A **627**, 645 (1997); M. Guidal, J.M. Laget, and M. Vanderhaeghen, Phys. Rev. C **61**, 025204.

[34] R. Nasseripour *et al. (CLAS Collaboration)*, Phys. Rev. C **77**, 065208 (2008).

[35] G. Knöchlein, D. Drechsel, and L. Tiator, Z. Phys. A **352**, 327 (1995).

[36] J.M. Laget, Nucl. Phys. A **579**, 333 (1994).

[37] C.J. Bebek *et al.*, Phys. Rev. D **15**, 3082 (1977).

[38] G.F. Chew *et al.*, Phys. Rev. **106**, 1345 (1957).

[39] B.E. Bonner *et al.*, Phys. Rev. D **38**, 729 (1988).

[40] R. Gatto, Phys. Rev. **109**, 610 (1957).

[41] E.W. Hughes and R. Voss, Ann. Rev. of Nucl. and Part. Sci. **49**, 303 (1999).

[42] T. Mart, code from private communication.

[43] B.A. Mecking *et al.*, Nucl. Inst. and Meth. A **503**, 513 (2003).

[44] M.D. Mestayer *et al.*, Nucl. Inst. and Meth. A **449**, 81 (2000).

[45] G.S. Adams *et al.*, Nucl. Inst. and Meth. A **465**, 414 (2001).

[46] E.S. Smith *et al.*, Nucl. Inst. and Meth. A **432**, 265 (1999).

[47] M. Amarian *et al.*, Nucl. Inst. and Meth. A **460**, 239 (2001).

[48] M.U Mozer and D.S. Carman, CLAS-Note 02-005, see http://www.jlab.org/Hall-B/notes/.

[49] D.S. Carman and B.A. Raue, CLAS-Note 02-018, see http://www.jlab.org/Hall-B/notes/.

[50] CLAS physics database, http://clasweb.jlab.org/physicsdb.

[51] M. Guidal, private communication.

[52] T. Corthals, private communication.

[53] B. Saghai, Nucl. Phys. A **639**, 217 (1998).

[54] S. Frullani, F. Garibaldi, J. LeRose, P. Markowitz, and T. Saito, JLab experiment E94-108, "Electroproduction of Kaons up to $Q^2 = 3$ GeV^2".

[55] W.R. Frazer, Phys. Rev **115**, 1763 (1959).

[56] N. Isgur and J. Paton, Phys. Rev. D **31**, 2910 (1985).

[57] A. LeYaouanc *et al.*, Phys. Rev. D **8**, 2223 (1973).

[58] D.S. Carman, T.S.-H. Lee, M.D. Mestayer, and R.A.Schumacher, CERN Courier **47** No.7, 32 (2007).

[59] Z. Liang and C. Boros, Phys. Rev. D **61**, 117503 (2000).

[60] N. Kochelev, Phys. Rev. D **75**, 077503 (2007).

[61] R. Schumacher, Eur. Phys. J A **35**, 299 (2008).

[62] T.-S.H. Lee, private communication.

[63] Jefferson Laboratory Excited Baryon Analysis Center (EBAC), see http://ebac-theory.jlab.org/main.htm.

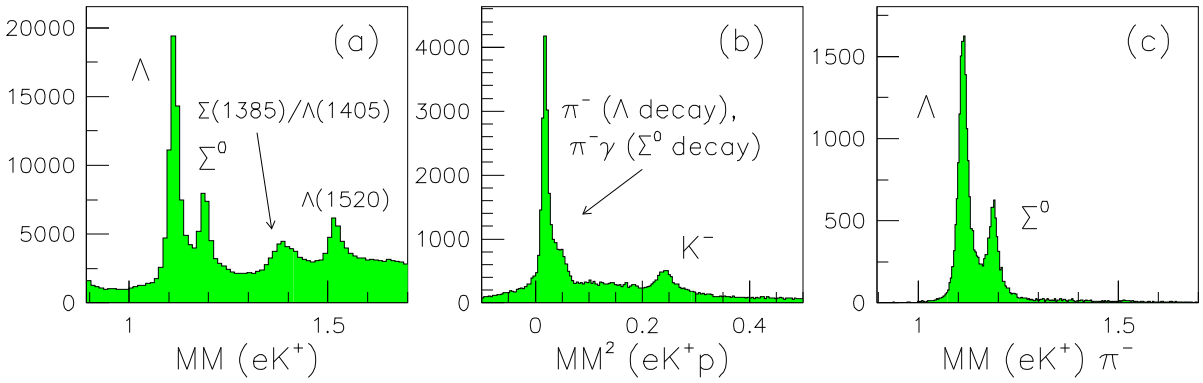
(a)
Λ
Σ(1385)/Λ(1405)
Σ⁰
Λ(1520)
MM (eK⁺)
(b)
π⁻ (Λ decay),
π⁻γ (Σ⁰ decay)
K⁻
MM² (eK⁺p)
(c)
Λ
Σ⁰
MM (eK⁺) π⁻

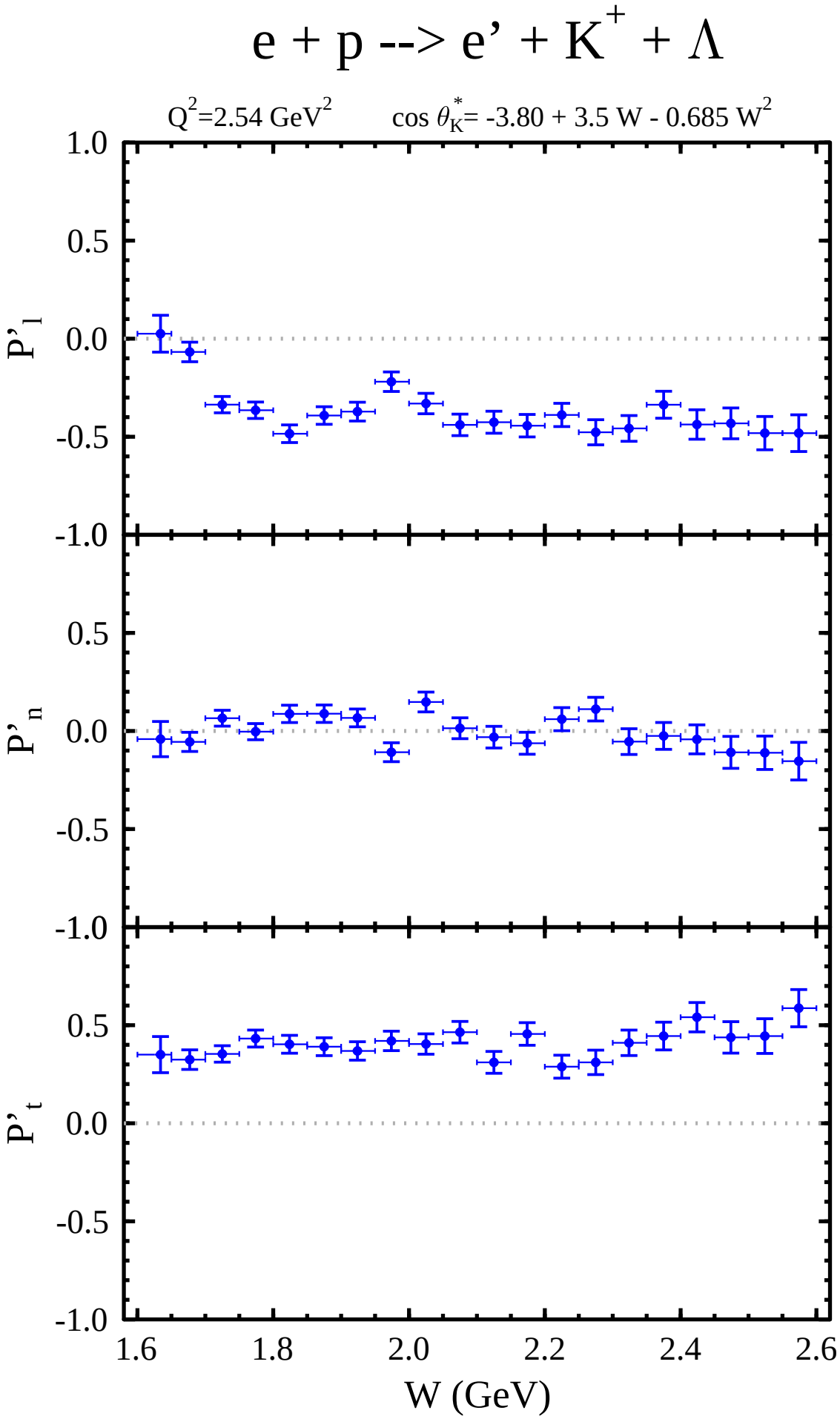

asmqth sort

e1-6 data set

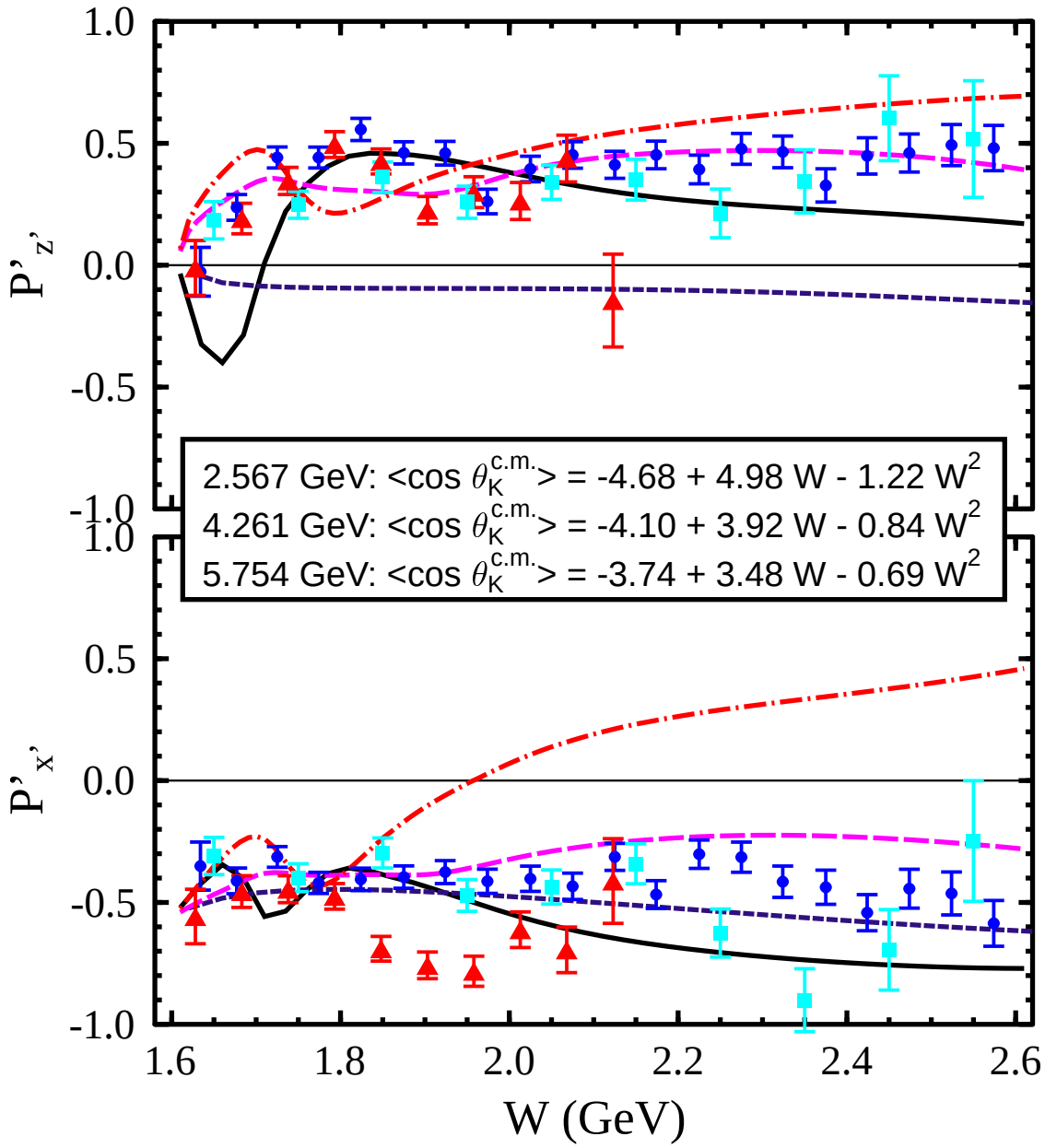
1.0
0.5
0.0
-0.5
-1.0
P'z'
2.567 GeV: <cos θK c.m.> = -4.68 + 4.98 W - 1.22 W2
4.261 GeV: <cos θK c.m.> = -4.10 + 3.92 W - 0.84 W2
5.754 GeV: <cos θK c.m.> = -3.74 + 3.48 W - 0.69 W2
P'x'
1.6
1.8
2.0
2.2
2.4
2.6
W (GeV)

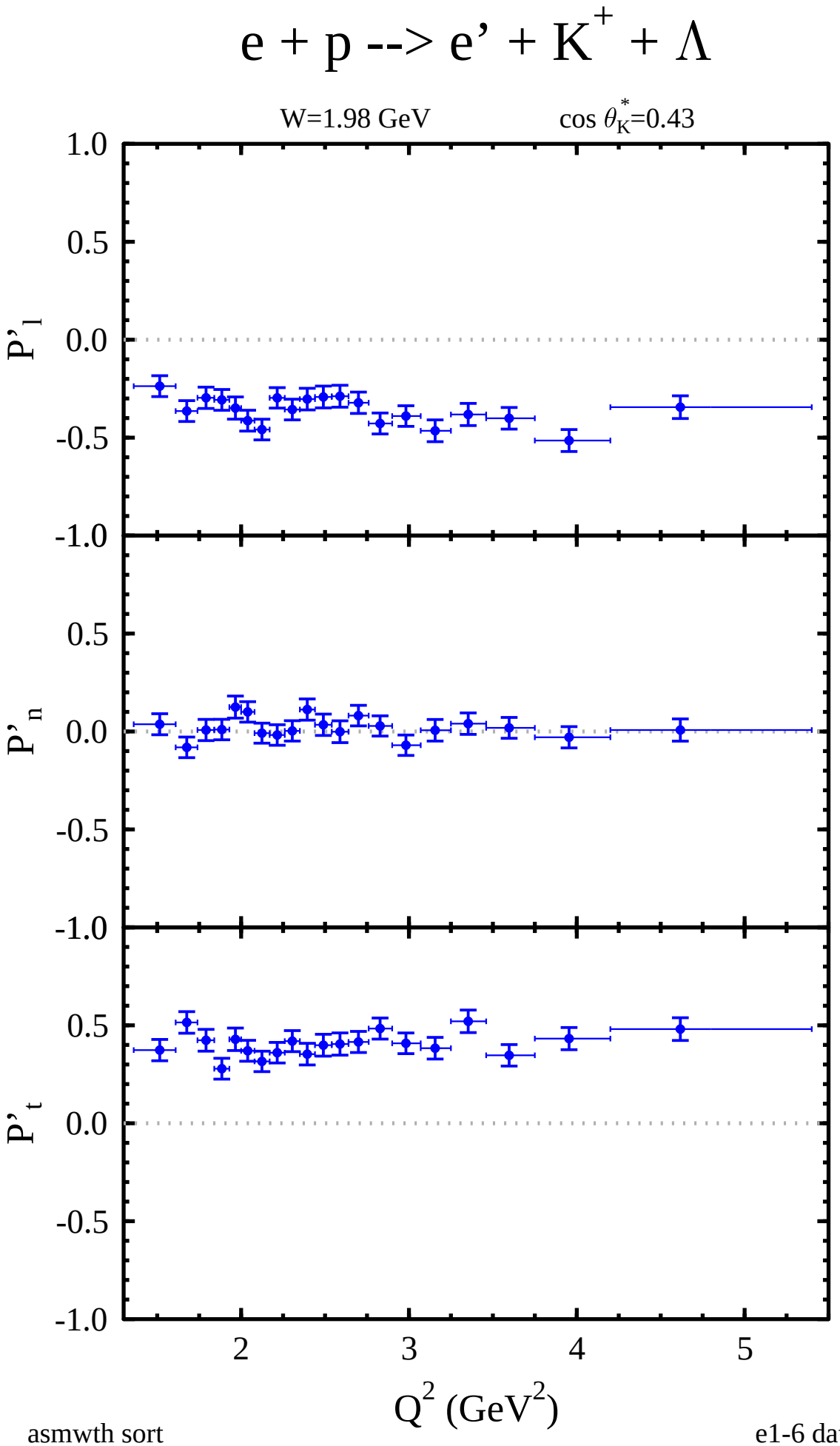
e + p --> e' + K+ + Λ
W=1.98 GeV
cos θ*K=0.43
P'l
P'n
P't
1.0
0.5
0.0
-0.5
-1.0
2
3
4
5
Q2 (GeV2)
asmwth sort
e1-6 data set